

OPEN ACCESS

The Effect of Liquid Saturation Transients on PEM Fuel Cell Impedance: Inductive Loop and Instability of Catalyst Layer Operation

To cite this article: Ying Sun et al 2024 J. Electrochem. Soc. 171 074506

View the article online for updates and enhancements.

You may also like

- Low-frequency Inductive Loop and Its Origin in the Impedance Spectrum of a Graphite Anode

Arun Thapa and Hongwei Gao

- Numerical Study of the Impact of Two-Phase Flow in the Anode Catalyst Layer on the Performance of Proton Exchange Membrane Water Electrolysers
 M. Moore, M. Mandal, A. Kosakian et al.
- Pore-Water Morphological Transitions in Polymer Electrolyte of a Fuel Cell
 G. S. Hwang, M. Kaviany, J. H. Nam et al.





The Effect of Liquid Saturation Transients on PEM Fuel Cell Impedance: Inductive Loop and Instability of Catalyst Layer Operation

Ying Sun, 1,2,z Thomas Kadyk, 1,3 Andrei Kulikovsky, 1,2 and Michael Eikerling 1,2,3

We report a physics—based model for the electrochemical impedance of a PEM fuel cell cathode. The model takes into account the transient behavior of oxygen and proton transport in the cathode catalyst layer caused by a variation of the liquid saturation with cell current. Transients of the catalyst layer oxygen diffusivity result in a second capacitive arc in the Nyquist spectrum, while proton conductivity transients lead to the formation of an inductive loop. In the range of capillary pressures in which the liquid saturation in the catalyst layer is independent of the *capillary pressures*, the loop does not form. A stability analysis of a reduced system of equations reveals that the static limit of inductive loop is unstable with respect to spatial perturbations, implying that the post–oscillatory steady state is unattainable. Possible scenarios of instability development are discussed.

© 2024 The Author(s). Published on behalf of The Electrochemical Society by IOP Publishing Limited. This is an open access article distributed under the terms of the Creative Commons Attribution 4.0 License (CC BY, http://creativecommons.org/licenses/by/4.0/), which permits unrestricted reuse of the work in any medium, provided the original work is properly cited. [DOI: 10.1149/1945-7111/ad5efd]

, ref

Deference ovvigen pressure Do

Dimensionless parameter, Eq. E8Angular frequency of the AC signal, s^{-1}

Manuscript submitted January 16, 2024; revised manuscript received June 30, 2024. Published July 15, 2024.

Nomonelature

^zE-mail: Y.Sun@fz-juelich.de; A.Kulikovsky@fz-juelich.de

	Nomenclature	$p_{O_2}^{rej}$	Reference oxygen pressure, Pa
		n	Liquid water pressure in the CCL, Pa
~	Marks dimensionless variables	p_L^{ref}	Reference liquid water pressure, Pa
$b_{\underline{}}$	ORR Tafel slope, V	p_{cell}	Overall pressure,Pa
C_{dl}	Double layer capacitance, F cm ⁻³	Q_{ORR}	ORR rate, A cm ⁻³
D_b	Oxygen diffusivity in the GDL, cm ² s ⁻¹	Q_{lv}	Rate of vaporization, A cm ⁻³
$D_{b,d}$	Oxygen diffusivity in the dry GDL, cm ² s ⁻¹	r	Pore radius, µm
D_{ox}	Oxygen diffusivity in the CCL, cm ² s ⁻¹	R	Gas constant, J/(K mol)
$D_{ox,d}$	Oxygen diffusivity in the dry CCL, cm ² s ⁻¹	RH	Relative humidity,
D_{v}	Water vapor diffusivity in the CCL, cm ² s ⁻¹	S	CCL liquid saturation,
e_0	The elementary charge, C	s_0	Reference liquid saturation,
F	Faraday constant, $C \text{ mol}^{-1}$	T	Cell temperature, K
i	Imaginary unit	t	Time, s
i_*	Volumetric exchange current density, A cm ⁻³	t_*	Characteristic time, s
J_b	Oxygen molar flux in GDL, mol cm $^{-2}$ s $^{-1}$	V_m	Molar volume of liquid water, m ³ mol ⁻¹
J_{ν}	Water vapor molar flux in CCL, mol cm ⁻² s ⁻¹	X_p	Porosity of CCL
J_L	Liquid water molar flux in CCL, mol cm ⁻² s ⁻¹	$x^{'}$	Coordinate through cell, m
J_{O_2}	Oxygen molar flux in CCL, mol cm ⁻² s ⁻¹	Z	Electrochemical impedance, Ohm cm ²
J_p	Local proton current density, A cm ⁻²	Subscripts:	
J _{cell}	Cell current density, A cm ⁻²	0	membrane/CCL interface
j	Local proton current density in CCL, A cm ⁻²	1	CCL/GDL interface
j _*	Characteristic current density, A cm ⁻²	b	GDL
K_L	Liquid water permeability, m ²	h	Channel
k_{pc}	Parameter determining slope in water retention	*	Characteristic value
,	curve, Pa	Superscripts:	
k_{σ}	Constant of proton conductivity vs. saturation, S m ⁻¹	0	Steady state value
1		1	Small amplitude perturbation
k_L	Liquid transport coefficient, mol m ⁻¹ Pa ⁻¹ s ⁻¹	Greek:	
k_{lv}	Vaporization coefficient, mol m ⁻³ Pa ⁻¹ s ⁻¹	α , β	Dimensionless parameters, Eq. E8
l_t	CCL thickness, m	γ , ε	Dimensionless parameters, Eq. B8
l_b	GDL thickness, m	η	ORR overpotential, V
$p_{v_{s}}$	Water vapor partial pressure, Pa	μ	Dimensionless parameter, Eq. B8
p_{v}^{s}	Saturated vapor pressure at 80 °C, Pa Capilliary pressure, Pa	μ_w	Viscosity of liquid water, Pa s
p_c		κ	Vaporization rate constant, atm ⁻¹ m ⁻² s ⁻¹
p_l	Liquid phase pressure, Pa	$\xi^{ m lv}$	Vaporization interfacial area factor
p_g	Gas phase pressure, Pa	ν	Air kinematic viscosity, m ² s ⁻¹
p_b	Oxygen pressure in the GDL, Pa Oxygen pressure in the CCL, Pa	ρ	Air density, kg m ⁻³
p_{O_2}	Oxygen pressure in the CCL, i a	σ	CCL proton conductivity, S m ⁻¹
		σ_*	Reference CCL proton conductivity, S m ⁻¹

¹ Forschungszentrum Jülich GmbH, Theory and Computation of Energy Materials (IEK–13), Institute of Energy and Climate Research, D–52425 Jülich, Germany

²RWTH Aachen University, Chair of Theory and Computation of Energy Materials, Faculty of Georecources and Materials Engineering, D–52062 Aachen, Germany

³ Jülich Aachen Research Alliance, JARA Energy, D–52425 Jülich, Germany

Electrochemical impedance spectroscopy is a unique non-invasive and non-destructive tool for operando testing of PEM fuel cells. Measuring impedance spectra with modern EIS-equipment is a routine procedure. Frequency-dependent EIS data allow one to separate contributions of different transport and kinetic processes to cell performance.

The typical Nyquist spectrum of a PEM fuel cell contains a number of overlapping arcs representing the oxygen reduction reaction (ORR) as well as oxygen and proton transport processes inside the cell. In addition, in some cases EIS spectra exhibit a low-frequency (LF) inductive loop. The nature of this loop has long been discussed in the literature; yet, it is not fully understood. The frequencies of the LF loop fall into the range 10^{-3} – 10^{-1} Hz, which lies well below characteristic frequencies of ORR and oxygen transport in porous layers. The only process manifesting itself at frequencies around 0.1 Hz is oxygen transport in the channel, which, however, does not exhibit inductive behavior. Apparently, in a cell operated under constant air flow rate another slow process must be responsible for this feature.

Three suspects are usually named as possibly being responsible for the occurrence of the inductive loop at low frequency: carbon monoxide poisoning, side reactions with intermediates, and water transport in the membrane. Experiments of Wagner and Gülzow⁴ have shown that CO poisoning of the PEMFC cathode could be responsible for the inductive loop. However, with the usage of ultrapure gases, the remaining two candidates seem more likely culprits. For side reactions with intermediates, Antoine, Bultel and Durand⁵ and later Makharia, Mathias, and Baker⁶ explained the inductive behavior by slow dynamics of ORR intermediates on the Pt surface. Roy and Orazem⁷ and Roy, Orazem and Tribollet⁸ attributed the LF loop to the formation of hydrogen peroxide or Pt dissolution. Setzler and Fuller⁹ reported a physics-based impedance model that accounted for Pt oxidation and conjectured the formation of the LF loop due to this process. A similar, though simpler model has been developed by Gerling et al. 10 As for water transport in the membrane, Schneider¹¹ observed a large inductive loop at low temperature and low relative humidity, originating from water generation. Wiezell¹² reported a model according to which water transport in the membrane results in the LF loop and the size of the loop is in positive correlation with membrane thickness. Holmström¹³ attributed the LF loop in their experiments to the water transport characteristics of the membrane. Kosakian¹⁴ utilized a physics-based MEA model to demonstrate that the occurrence of the inductive loop can be attributed to the dynamics of membrane hydration. A detailed literature review of the effect and possible origins of a LF loop has been provided by Pivac and Barbir, 15 suggesting that for different operating conditions, different mechanisms may come into play. Water transport may play a vital role at low relative humidity and low temperature while side reactions could come into play under fully humidified conditions. Meyer and Zhao¹⁶ experimentally demonstrated the formation of an LF loop induced by variation of the inlet air flow velocity in-phase with the applied AC current perturbation.

Recently, Kulikovsky¹⁷ developed a model of the PEMFC impedance that takes into account an empirical dependence of the proton conductivity in the cathode catalyst layer (CCL) on the cell current due to a slow variation of the ionomer phase humidification in the CCL. The model leads to an inductive loop with the loop diameter proportional to the cell current. The experimental studies of Gerling et al.¹⁰ provide an evidence in favor of this mechanism. It is worth mentioning that the loop apparently reduces the total cell static resistivity, meaning that the effect is beneficial for the cell performance.

Below, we report a model for the PEMFC cathode impedance that takes into account the effect of water dynamics on oxygen and proton transport coefficients in the CCL. The model predicts an inductive loop that forms due to the slow relaxation of the CCL proton conductivity. In the limit of $\omega \rightarrow 0$, the loop tends to the static cell resistivity, which is lower than the unperturbed static resistivity.

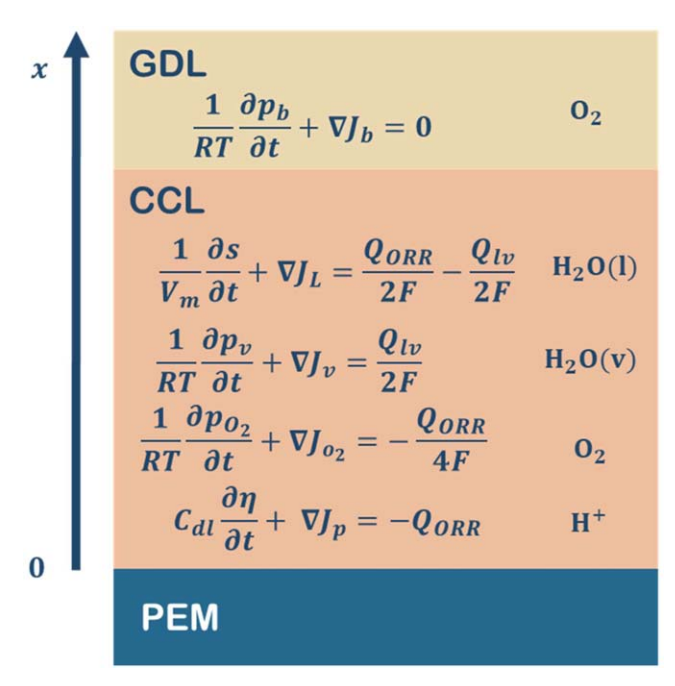


Figure 1. Schematic of the cathode side of a PEMFC, including cathode catalyst layer (CCL) and gas diffusion layer(GDL). The governing equations for water, oxygen and proton transport are given in the corresponding layers.

However, stability analysis of the reduced system of equations shows that this type of "post-inductive" steady state is unreachable due to system instability with respect to spatial perturbations.

We show that the size of the loop is determined by the dependence of the liquid saturation, s, on the capillary pressure, p_c . In the range of p_c , where s is independent of p_c , the inductive loop does not form. In this case, relaxation of the CCL oxygen diffusivity results in a second low–frequency capacitive arc in the Nyquist spectrum, which increases the cell static resistivity.

To simplify paper reading, details of all mathematical transformations are given in Appendices. In the bulk of the paper, we formulate the basic transport equations and proceed to results and discussions.

Model

General assumptions.—The schematic model domain and basic transport equations are shown in Fig. 1. The model includes the processes of liquid water permeation, vaporization, and water vapor diffusion in CCL. It takes into account oxygen transport in CCL and gas diffusion layer (GDL), and proton transport in CCL. All aforementioned processes are assumed to occur in the through–plane direction (along the *x*-axis in Fig. 1).

The following basic assumptions are employed:

- the air flow stoichiometry is infinite, thus the oxygen concentration in the channel is uniform justifying a one-dimensional treatment of oxygen transport in through-plane direction.
- the proton conductivity, σ , and oxygen diffusivity, D_{ox} , depend on the liquid water saturation in the CCL.
- the fluxes of water and oxygen through the CCL/membrane interface are negligible. The absence of oxygen flux is justified with the gas-tightness of the PEM. The absence of water flux implies that the diffusive flux of water produced in the oxygen reduction reaction (ORR) counterbalances the electroosmotic water flux from the anode side. This assumption simplifies the model; in future work, it will be relaxed.
- the water saturation in the GDL is constant and uniform throughout the GDL thickness dimension.

Basic transport equations.—Assuming that water in the ORR is produced in liquid form, the transport of liquid and gaseous water can be described by the following set of equations. The liquid water saturation in the CCL, s, is determined by

$$\frac{1}{V_{vv}}\frac{\partial s}{\partial t} + \nabla J_L = \frac{Q_{ORR}}{2F} - \frac{Q_{lv}}{2F},\tag{1}$$

where V_m is the molar volume of water, t time, J_L the liquid water molar flux in the CCL, Q_{ORR} the ORR rate, Q_{Iv} the volumetric rate of water vaporization, and F Faraday constant. For the water vapor partial pressure p_v in the CCL, we have

$$\frac{1}{RT}\frac{\partial p_{\nu}}{\partial t} + \nabla J_{\nu} = \frac{Q_{l\nu}}{2F},$$
 [2]

where J_{ν} is the water vapor molar flux in the CCL, R gas constant, T absolute temperature. The oxygen mass transport equation in terms of partial pressure p_{O_2} is

$$\frac{1}{RT}\frac{\partial p_{O_2}}{\partial t} + \nabla J_{O_2} = -\frac{Q_{ORR}}{4F},\tag{3}$$

where J_{O_2} is the oxygen molar flux in the CCL. The proton charge conservation equation reads

$$C_{dl}\frac{\partial \eta}{\partial t} + \nabla J_p = -Q_{ORR},\tag{4}$$

where C_{dl} is the double layer capacitance, η the ORR overpotential, and J_p the local proton current density. The oxygen partial pressure p_b in the GDL is obtained from

$$\frac{1}{RT}\frac{\partial p_b}{\partial t} + \nabla J_b = 0,$$
 [5]

where J_b is the oxygen molar flux in the GDL. In this work, we assume that liquid water is evaporated in the CCL and water vapor is rapidly removed through the GDL. The equations for water transport in the GDL will be incorporated in the next version of the model.

Fluxes and reaction rates.—Liquid water flux follows Darcy law

$$J_L = -\frac{K_L}{V_m \mu_{\nu}} \frac{\partial p_L}{\partial x},\tag{6}$$

where p_L is the liquid water pressure in the CCL, K_L the liquid water permeability, and μ_w the water viscosity. Water vapor flux is described by Fick law

$$J_{\nu} = -\frac{D_{\nu}}{RT} \frac{\partial p_{\nu}}{\partial x},\tag{7}$$

where D_{v} is the water vapor diffusivity.

Oxygen transport in the CCL and GDL conforms to Fick law

$$J_{O_2} = -\frac{D_{ox}}{RT} \frac{\partial p_{O_2}}{\partial x},\tag{8}$$

$$J_b = -\frac{D_b}{RT} \frac{\partial p_b}{\partial x},\tag{9}$$

where D_{ox} , D_b are the oxygen diffusivities in CCL and GDL, respectively.

The proton transport follows Ohm law

$$J_p = -\sigma \frac{\partial \eta}{\partial x},\tag{10}$$

where σ is proton conductivity.

The ORR rate is given by Tafel law

$$Q_{ORR} = i_* \left(\frac{p_{O_2}}{p_{O_2}^{ref}} \right) \exp\left(\frac{\eta}{b} \right),$$
 [11]

where $p_{O_2}^{ref}$ is the reference partial oxygen pressure, b the ORR Tafel slope, and i_* the volumetric exchange current density.

The rate of vaporization is given by

$$Q_{lv} = \frac{2e_0 \kappa \xi^{lv}}{l_t} (p_v^s - p_v),$$
 [12]

where e_0 is the elementary charge, κ the rate constant of evaporation, ξ^{lv} the vaporization interfacial area factor, l_t the thickness of the catalyst layer, and p_v^s the saturation vapor pressure.

The substitution of J_L , J_v , J_{O_2} , J_p , J_b , Q_{ORR} and Q_{lv} into the transport equations is described in Appendix A. To simplify calculations, we transform equations into dimensionless form; the details are given in Appendix B. The steady–state scenario is discussed in Appendix C. The analysis of the transient equations is presented in Appendix D.

Saturation, capillary pressure and the transport parameters.— To characterize the liquid saturation in the CCL, s, we introduce the water retention curve (WRC), which is the relation between capillary pressure and liquid saturation, $s(p_c)$. The capillary pressure, p_c , is the difference between the liquid phase pressure, p_l , and the gas phase pressure, p_g ,

$$p_c = p_1 - p_q. ag{13}$$

The relation between water retention curve and pore size distribution (PSD) has been discussed in recent works of Kusoglu et al., ¹⁸ Zhang et al., ¹⁹ and Olbrich et al. ²⁰ The curve $s(p_c)$ serves as input for the current model. The CCL exhibits mixed wettability, characterized by the relationship between the contact angle and 90°. Hydrophilic pores with contact angle smaller than 90°, adhere to a bimodal lognormal PSD, akin to the model of the CCL pore space morphology described by Eikerling.²¹ In contrast, hydrophobic pores, featuring a contact angle larger than 90°, follow a monomodal log-normal PSD. Similar methodologies have been employed by Weber et al., ²² Zhou et al.,²³ and Kosakian et al.²⁴ Given the average contact angle for hydrophobic and hydrophilic pores, the water retention curve can be derived from the PSD, as elaborated in Zhang et al. 19 and Olbrich et al.²⁰ However, due to the composite nature of pore-forming CCL constituents (Pt, carbon, and ionomer), pore wettability is inherently mixed, resulting in a continuous distribution of contact angles. Consequently, in addition to employing mixed wettability for constructing the water retention curve an alternative model, as proposed by Olbrich et al.²⁰ offers a novel avenue for its determination. This model, accounting for the ink composition and intrinsic material properties, presents a promising approach to calculating WRC with statistical distributions of wetting properties. WRC generated with the model of Olbrich et al. can be fitted using

$$s = a + \frac{(1-a)}{2} \left(1 + \tanh\left(\frac{p_c - p_{c,0}}{k_{pc}}\right) \right).$$
 [14]

This approach is used below. All three aforementioned curves are shown in Fig. 2.

We employ a macro-homogeneous model, where gaseous and liquid water are not separated in space. They share the same representative elementary volume. It is assumed that in this volume, some domains of the ionomer are in contact with liquid water, while the other domains are in contact with water vapor. Overall, ionomer proton conductivity is assumed to be proportional to liquid saturation. A linear relation between proton conductivity, σ , and liquid

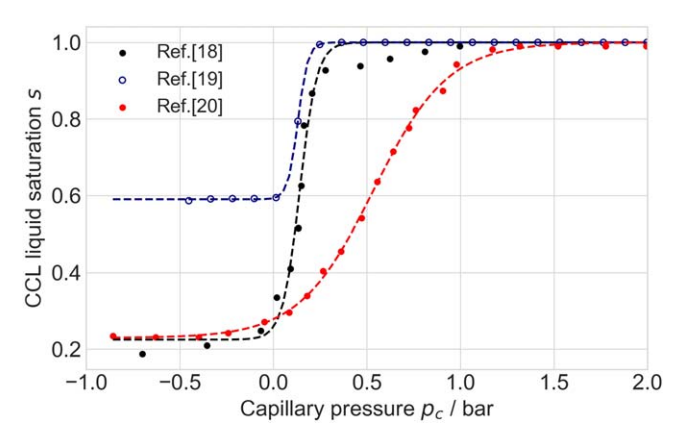


Figure 2. CCL water retention curves from Zhang et al.¹⁹ (open circles), Kusoglu et al.¹⁸ (black points), and Olbrich et al.²⁰ (red points). Solid line—the function Eq. 14 fitted to the data. Parameters for the red curve in Eq. 14 are: a=0.2293, p_{c.0} = 0.5361 bar, k_{pc} = 0.3984 bar.

water saturation, s, is thus employed for the CCL, 25

$$\sigma = k_{\sigma} s, \tag{15}$$

where k_{σ} is a proportionality constant. Experiments²⁶ show that to good approximation, the CCL oxygen diffusivity D_{ox} changes with s according to

$$D_{ox} = D_{ox,d}(1-s)^2,$$
 [16]

where $D_{ox,d}$ is the "dry" value of CCL oxygen diffusivity.

Electrochemical impedance.—The basic transport Eqs. 1–5 were nondimensionalized, linearized and Fourier–transformed to derive a system of linear equations for the small perturbation amplitudes \tilde{s}^1 , \tilde{p}_{ν}^1 , $\tilde{p}_{O_2}^1$, $\tilde{\eta}^1$, \tilde{p}_b^1 in the $\tilde{\omega}$ –space (Appendix B, D). The cathode electrochemical impedance Z is given by

$$Z = -\frac{\eta^1}{\sigma \partial \tilde{\eta}^1 / \partial \tilde{x}} \bigg|_{\mathbf{r} = 0} . \tag{17}$$

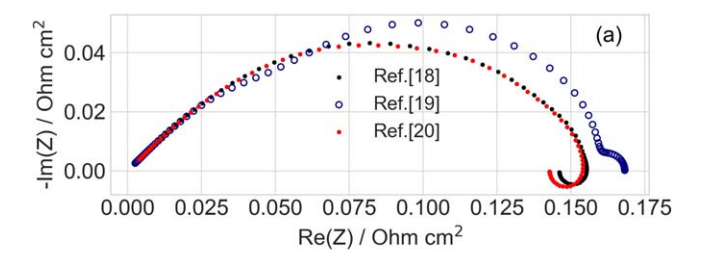
We derive Z by solving the system of Eqs. D2–D5 assuming zero oxygen pressure variation in the channel, $\tilde{p}_h^1 = 0$. Note that water vapor transport in the GDL is taken into account by Eq. 5. We assume that liquid water is evaporated in the CCL. Here and below, superscripts 0 and 1 represent static values and small perturbation amplitudes in ω -space, respectively.

Results and Discussion

EIS spectra are sensitive to variation in CCL water content, which affects the proton conductivity and oxygen diffusivity. Under the assumption of uniform s though the GDL thickness, EIS does not "feel" variations of the GDL oxygen diffusivity with water content. This variation could be registered in EIS experiments, if the GDL liquid saturation is non-uniform. Nonetheless, the static value of GDL oxygen diffusivity D_b contributes to EIS spectra.

The cathode impedance Z for the base-case parameters in Table I is depicted in Fig. 3. As can be seen, an inductive loop forms in the Nyquist spectra for the two water retention curves from Ref. [18] and Ref. [20]. The zoomed inductive loop obtained with the retention curve from Ref. [20] is shown in Figure 4a. We will rationalize the spectra in Fig. 3 by considering the limiting cases.

Limiting case: uniform and constant liquid saturation.—We consider first the limiting case of time-independent liquid saturation ($s^1 = 0$). In this case, the liquid saturation is static and uniform throughout the CCL depth, making oxygen diffusivity and proton



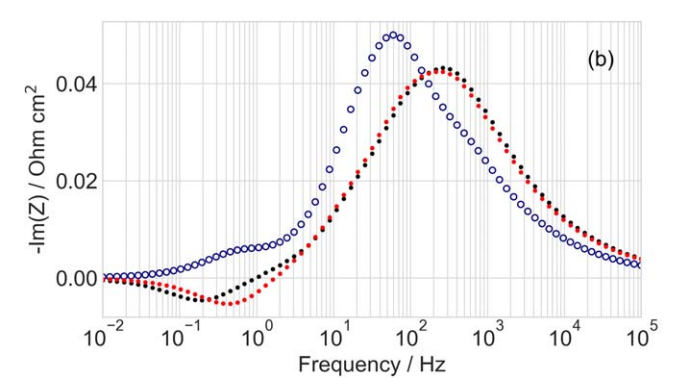


Figure 3. (a) Nyquist spectra of electrochemical impedance *Z*, Eq. 17, calculated from Eqs. D2–D5 for the parameters in Table I with different water retention curves, where open circles are from Zhang et al., ¹⁹ black dots from Kusoglu et al., ¹⁸ and red dots from Olbrich et al. ²⁰ (b) Bode plots describing the frequency dependence of the imaginary part of the impedance in (a). Parameters are listed in Table I.

conductivity independent of time: $D_{ox}^1 = 0$, $\sigma^1 = 0$. The governing Eqs. D2–D5 reduce to Eqs. F1–F4. The Nyquist plot resulting from the numerical solution of Eqs. F1–F4 with the parameters from Table I does not exhibit an inductive loop (Fig. 4b). It is, thus, clear that the inductive arc in Figs. 3, 4a originates from the relaxation of one of the CCL transport parameters. It is advisable to separate the contributions of variable σ and D_{ox} to cell impedance, as discussed in the sections that follow.

Limiting cases of constant oxygen diffusivity and/or proton conductivity.—The characteristic time of liquid saturation variation is above 1 s, hence corresponding features are seen in the low-frequency (LF) domain of the spectra. The LF parts of the Nyquist spectra for all possible combinations of constant and/or time-dependent D_{ox} and σ are compared in Fig. 4.

In the case of transient σ , but time-independent D_{ox} ($D_{ox}^1 = 0$), the governing Eqs. D2–D5 reduce to Eqs. F5–F8, leading to the spectrum in Fig. 4c. As can be seen, the inductive loop is more pronounced (cf. Figs. 4a and 4c) and the static resistance of the cell is reduced by 10 mOhm cm² compared to Fig. 4a. Thus, the saturation–dependent proton conductivity results in the inductive arc, which agrees with the finding of Kulikovsky.¹⁷ Calculations show that the diameter of the inductive loop increases with current density in agreement with the analysis in Ref.[17]. However, in this work we employ a physics-based model to describe water transport, while Kulikovsky¹⁷ used an empirical relation between proton conductivity and current density.

In the case of transient D_{ox} but time-independent σ ($\sigma^1 = 0$), Eqs. D2–D5 reduce to Eqs. F9–F12. The numerical solution to Eqs. F9–F12 with the parameters from Table I gives the spectrum in Fig. 4d. The transient oxygen diffusivity gives rise to a second low–frequency capacitive arc. Thus, within the scope of the model above, the sole reason for the inductive loop is the saturation–dependent relaxation of σ .

The role of the retention curve slope.—Equation 14 shows that the slope of the WRC is determined by the parameter k_{pc} : with k_{pc} growth, the retention curve slope decreases. This parameter may

Table I	The	hase_case	cell	narameters	nsed	in	calculations	
rabie i.	1 110	Dase-Case	cen	Dai ameters	useu	ш	Calculations	•

Faraday constant F 96485 C mol ⁻¹ Temperature T 353 K Gas constant R 8.314 J/(K mol) Saturated vapor pressure at 80 °C at flat liquid-gas interface $p_s^{-p_s}$ 0.446 × 10 ⁵ Pa Reference coxygen pressure $p_s^{-p_s}$ $(1 - RH) × p_s^p × 0.21$ Pa Reference liquid water pressure $p_s^{-p_s}$ $(1 - RH) × p_s^p × 0.21$ Pa Reference liquid water pressure $p_s^{-p_s}$ $(1 - RH) × p_s^p × 0.21$ Pa Reference liquid water pressure $p_s^{-p_s}$ $(1 - RH) × p_s^p × 0.21$ Pa Reference liquid water pressure $p_s^{-p_s}$ $(1 - RH) × p_s^p × 0.21$ Pa Dry GDL oxygen diffusivity D_s 1×10^{-8} m²s ⁻¹ Water vapor diffusivity D_s 5×10^{-8} m²s ⁻¹ Water vapor diffusivity D_s 5×10^{-8} m²s ⁻¹ Volumetric exchange current density i. 1×10^{-3} A m ⁻³ Tafel slope (V/exp) b 0.030 V Double la	Parameters	Symbol	Value	Unit
Gas constant R 8.314 J/(K mol) Saturated vapor pressure at 80 °C at flat liquid-gas interface p_s^{-1} 0.446 × 10 ⁵ Pa Reference oxygen pressure p_c^{-1} (1 - RH) × p_s^{-1} × 0.21 Pa Reference liquid water pressure p_t^{-1} 0.391 × 10 ⁵ Pa Reference liquid water pressure p_t^{-1} 0.391 × 10 ⁵ Pa Dry CCL oxygen diffusivity Do.x.d 1 × 10 ⁻⁸ m²s ⁻¹ Water vapor diffusivity D _ν 5 × 10 ⁻⁸ m²s ⁻¹ Water vapor diffusivity D _ν 5 × 10 ⁻⁸ m²s ⁻¹ Vater vapor diffusivity D _ν 5 × 10 ⁻⁸ m²s ⁻¹ Water vapor diffusivity D _ν 5 × 10 ⁻⁸ m²s ⁻¹ Vater vapor diffusivity D _ν 5 × 10 ⁻⁸ m²s ⁻¹ Vater vapor diffusivity D _ν 5 × 10 ⁻⁸ m²s ⁻¹ Volumetric exchange current density b 0.030 V Double layer capacitance C _{dl} 2 × 10 ⁷ F m ⁻³ CCI. Thickness l _t 10	Faraday constant	F	96485	C mol ⁻¹
Saturated vapor pressure at 80 °C at flat liquid-gas interface p_v^s 0.446×10^5 Pa Reference oxygen pressure p_{02}^{ref} $(1 - RH) \times p_v^s \times 0.21$ Pa Reference liquid water pressure p_t^{ref} 0.391×10^5 Pa Dry CCL oxygen diffusivity $D_{ox,d}$ 1×10^{-8} m^2s^{-1} Water vapor diffusivity D_v 5×10^{-8} m^2s^{-1} Dry GDL oxygen diffusivity $D_{b,d}$ 2×10^{-6} m^2s^{-1} Volumetric exchange current density i_s 1×10^3 $A \text{ m}^{-3}$ Volumetric exchange current density i_s 1×10^3 $A \text{ m}^{-3}$ Tafel slope (V/exp) b 0.030 V Double layer capacitance C_{dl} 2×10^7 $F \text{ m}^{-3}$ CCL Thickness l_t 10×10^{-6} m GDL Thickness l_t 10×10^{-6} m Liquid water premability K_L 1×10^{-18} m^2 Viscosity of liquid water V_m 1.8×10^{-5} m^3 <	Temperature	T	353	K
Reference oxygen pressure p_{O2}^{ref} $(1-RH) \times p_y^y \times 0.21$ Pa Reference liquid water pressure p_L^{ref} 0.391×10^5 Pa Dry CCL oxygen diffusivity $D_{ox,d}$ 1×10^{-8} m^2s^{-1} Water vapor diffusivity D_v 5×10^{-8} m^2s^{-1} Dry GDL oxygen diffusivity $D_{b,d}$ 2×10^{-6} m^2s^{-1} Volumetric exchange current density i_s 1×10^3 $A \text{ m}^{-3}$ Tafel slope (V/exp) b 0.030 V Double layer capacitance C_{dl} 2×10^7 F m ⁻³ CCL Thickness l_t 10×10^{-6} m GDL Thickness l_t 10×10^{-6} m GDL Thickness l_t 10×10^{-6} m Liquid water permeability K_L 1×10^{-18} m^2 Wolar volume of liquid water V_m 1.8×10^{-5} m^3 mol ⁻¹ Viscosity of liquid water V_m 1.6×10^{-19} C Vaporization rate constant K_L <	Gas constant	R	8.314	J/(K mol)
Reference liquid water pressure $p_L^{\rm ref}$ 0.391×10^5 Pa Dry CCL oxygen diffusivity $D_{ox,d}$ 1×10^{-8} m^2s^{-1} Water vapor diffusivity D_V 5×10^{-8} m^2s^{-1} Dry GDL oxygen diffusivity $D_{b,d}$ 2×10^{-6} m^2s^{-1} Volumetric exchange current density i_* 1×10^3 $A m^{-3}$ Tafel slope (V/exp) b 0.030 V Double layer capacitance C_{dl} 2×10^7 $F m^{-3}$ CCL Thickness l_* 10×10^{-6} m GDL Thickness l_* 190×10^{-6} m GDL Thickness l_* 190×10^{-6} m Liquid water permeability K_L 1×10^{-18} m^2 Wolar volume of liquid water V_m 1.8×10^{-5} m^3 mol $^{-1}$ Viscosity of liquid water μ_w 8.9×10^{-4} Pa as Elementary charge e_0 1.6×10^{-19} C Vaporization rate constant κ	Saturated vapor pressure at 80 °C at flat liquid-gas interface	p_{v}^{s}	0.446×10^5	Pa
Reference liquid water pressure p_L^{ref} 0.391 × 10 ⁵ Pa Dry CCL oxygen diffusivity $D_{ox,d}$ 1 × 10 ⁻⁸ m²s ⁻¹ Water vapor diffusivity D_V 5 × 10 ⁻⁸ m²s ⁻¹ Dry GDL oxygen diffusivity $D_{b,d}$ 2 × 10 ⁻⁶ m²s ⁻¹ Dry GDL oxygen diffusivity $D_{b,d}$ 2 × 10 ⁻⁶ m²s ⁻¹ Volumetric exchange current density i* 1 × 10 ³ A m ⁻³ Tafel slope (V/exp) b 0.030 V Double layer capacitance C_{dl} 2 × 10 ⁷ F m ⁻³ CCL Thickness l_t 10 × 10 ⁻⁶ m GDL Thickness l_t 190 × 10 ⁻⁶ m Liquid water permeability K_L 1 × 10 ⁻¹⁸ m² Molar volume of liquid water V_m 1.8 × 10 ⁻⁵ m³mol ⁻¹ Viscosity of liquid water μ_w 8.9 × 10 ⁻⁴ Pa s Elementary charge e_0 1.6 × 10 ⁻¹⁹ C Vaporization rate constant ξ^{lv} 80 Constant ofp	Reference oxygen pressure	p_{O2}^{ref}	$(1 - RH) \times p_v^s \times 0.21$	Pa
Dry CCL oxygen diffusivity $D_{ox,d}$ 1×10^{-8} m^2s^{-1} Water vapor diffusivity D_v 5×10^{-8} m^2s^{-1} Dry GDL oxygen diffusivity $D_{b,d}$ 2×10^{-6} m^2s^{-1} Volumetric exchange current density i_s 1×10^3 $A \text{ m}^{-3}$ Volumetric exchange current density i_s 1×10^3 $A \text{ m}^{-3}$ Tafel slope (V/exp) b 0.030 V Double layer capacitance C_{dl} 2×10^7 $F \text{ m}^{-3}$ CCL Thickness l_t 10×10^{-6} m GDL Thickness l_b 190×10^{-6} m Liquid water permeability K_L 1×10^{-18} m^2 Molar volume of liquid water V_m 1.8×10^{-5} $m^3 \text{mol}^{-1}$ Viscosity of liquid water μ_w 8.9×10^{-4} P_a Elementary charge e_0 1.6×10^{-19} C Vaporization rate constant κ 1.38×10^{17} P_a^{-1} Vaporization interfacial area	Reference liquid water pressure		0.391×10^{5}	Pa
Water vapor diffusivity D_v 5×10^{-8} m^2s^{-1} Dry GDL oxygen diffusivity $D_{b,d}$ 2×10^{-6} m^2s^{-1} Volumetric exchange current density i_* 1×10^3 A m ⁻³ Tafel slope (V/exp) b 0.030 V Double layer capacitance C_{dl} 2×10^7 F m ⁻³ CCL Thickness l_t 10×10^{-6} m GDL Thickness l_b 190×10^{-6} m Liquid water permeability K_L 1×10^{-18} m^2 Molar volume of liquid water V_m 1.8×10^{-5} m^3 mol ⁻¹ Viscosity of liquid water μ_w 8.9×10^{-4} P as Elementary charge e_0 1.6×10^{-19} C Vaporization rate constant κ 1.38×10^{17} Pa^{-1} m ⁻² s ⁻¹ Vaporization interfacial area factor ξ^{1v} 80 Constant of proton conductivity vs. saturation k_σ 1 Sm^{-1} Cell current density R 0.8	Dry CCL oxygen diffusivity		1×10^{-8}	${\rm m}^{2}{\rm s}^{-1}$
Dry GDL oxygen diffusivity $D_{b,d}$ 2×10^{-6} m^2s^{-1} Volumetric exchange current density i_* 1×10^3 A m ⁻³ Tafel slope (V/exp) b 0.030 V Double layer capacitance C_{dl} 2×10^7 F m ⁻³ CCL Thickness l_t 10×10^{-6} m GDL Thickness l_b 190×10^{-6} m GDL Thickness l_b 190×10^{-6} m Liquid water permeability K_L 1×10^{-18} m ² Molar volume of liquid water V_m 1.8×10^{-5} m³mol ⁻¹ Viscosity of liquid water μ_{wv} 8.9×10^{-4} Pa s Elementary charge e_0 1.6×10^{-19} C Vaporization rate constant κ 1.38×10^{17} Pa ⁻¹ m ⁻² s ⁻¹ Vaporization interfacial area factor ξ^{lv} 80 Sm ⁻¹ Cell current density j_{cell} 4×10^3 A m ⁻² Relative humidity RH 0.8 0.8	Water vapor diffusivity		5×10^{-8}	${\rm m}^{2}{\rm s}^{-1}$
Volumetric exchange current density i_* 1×10^3 A m ⁻³ Tafel slope (V/exp) b 0.030 V Double layer capacitance C_{dl} 2×10^7 F m ⁻³ CCL Thickness l_t 10×10^{-6} m GDL Thickness l_b 190×10^{-6} m GDL Thickness l_b 190×10^{-6} m Liquid water permeability K_L 1×10^{-18} m ² Molar volume of liquid water V_m 1.8×10^{-5} m³mol ⁻¹ Viscosity of liquid water μ_w 8.9×10^{-4} Pa s Elementary charge e_0 1.6×10^{-19} C Vaporization rate constant κ 1.38×10^{17} Pa^{-1} m ⁻² s ⁻¹ Vaporization interfacial area factor ξ^{lv} 80 80 Constant ofproton conductivity vs. saturation k_σ 1 80 Cell current density g_{cll} g_{cll} g_{cll} g_{cll} g_{cll} Cell current density g	Dry GDL oxygen diffusivity	$D_{b.d}$	2×10^{-6}	$\mathrm{m}^{2}\mathrm{s}^{-1}$
$ \begin{array}{c ccccccccccccccccccccccccccccccccccc$	Volumetric exchange current density		1×10^{3}	${\rm A~m}^{-3}$
CCL Thickness l_t 10×10^{-6} mGDL Thickness l_b 190×10^{-6} mLiquid water permeability K_L 1×10^{-18} m²Molar volume of liquid water V_m 1.8×10^{-5} $m^3 \text{mol}^{-1}$ Viscosity of liquid water μ_w 8.9×10^{-4} Pa sElementary charge e_0 1.6×10^{-19} CVaporization rate constant κ 1.38×10^{17} $Pa^{-1} \text{ m}^{-2} \text{ s}^{-1}$ Vaporization interfacial area factor ξ^{lv} 80Constant ofproton conductivity vs. saturation k_σ 1 Sm^{-1} Cell current density j_{cell} 4×10^3 $A \text{ m}^{-2}$ Relative humidity RH 0.8 Cathode pressure p_{cell} 1.5×10^5 p_{cell}	Tafel slope (V/exp)	b	0.030	
$ \begin{array}{c ccccccccccccccccccccccccccccccccccc$	Double layer capacitance	C_{dl}	2×10^{7}	${\rm F~m}^{-3}$
Liquid water permeability K_L 1×10^{-18} m^2 Molar volume of liquid water V_m 1.8×10^{-5} $m^3 \text{mol}^{-1}$ Viscosity of liquid water μ_w 8.9×10^{-4} Pa s Elementary charge e_0 1.6×10^{-19} C Vaporization rate constant κ 1.38×10^{17} $Pa^{-1} \text{ m}^{-2} \text{ s}^{-1}$ Vaporization interfacial area factor ξ^{lv} 80 Constant ofproton conductivity vs. saturation k_σ 1 Sm^{-1} Cell current density j_{cell} 4×10^3 $A \text{ m}^{-2}$ Relative humidity RH 0.8 Cathode pressure p_{cell} 1.5×10^5 p_{cell}	CCL Thickness	l_t	10×10^{-6}	m
Molar volume of liquid water V_m 1.8×10^{-5} $m^3 mol^{-1}$ Viscosity of liquid water μ_w 8.9×10^{-4} Pa s Elementary charge e_0 1.6×10^{-19} C Vaporization rate constant κ 1.38×10^{17} $Pa^{-1} m^{-2} s^{-1}$ Vaporization interfacial area factor ξ^{lv} 80 Constant ofproton conductivity vs. saturation k_σ 1 Sm^{-1} Cell current density j_{cell} 4×10^3 $A m^{-2}$ Relative humidity RH 0.8 Cathode pressure p_{cell} 1.5×10^5 p_{cell}	GDL Thickness	l_b	190×10^{-6}	m
Viscosity of liquid water $\mu_{w} = 8.9 \times 10^{-4} = Pa \text{ s}$ Elementary charge $e_{0} = 1.6 \times 10^{-19} = C$ Vaporization rate constant $\kappa = 1.38 \times 10^{17} = Pa^{-1} \text{ m}^{-2} \text{ s}^{-1}$ Vaporization interfacial area factor $\xi^{\text{lv}} = 80$ Constant of proton conductivity vs. saturation $k_{\sigma} = 1 = 1.5 \times 10^{3} = 1.5 \times 10^{5}$ Cell current density $RH = 0.8$ Cathode pressure $p_{\text{cell}} = 1.5 \times 10^{5} = Pa$	Liquid water permeability	K_L	1×10^{-18}	
Elementary charge e_0 1.6×10^{-19} C Vaporization rate constant κ 1.38×10^{17} Pa^{-1} m^{-2} s^{-1} Vaporization interfacial area factor ξ^{lv} 80 Constant of proton conductivity vs. saturation k_{σ} 1 Sm ⁻¹ Cell current density j_{cell} 4×10^3 A m ⁻² Relative humidity RH 0.8 Cathode pressure p_{cell} 1.5×10^5 Pa	Molar volume of liquid water	V_m	1.8×10^{-5}	$m^3 mol^{-1}$
Vaporization rate constant κ 1.38×10^{17} Pa^{-1} m $^{-2}$ s $^{-1}$ Vaporization interfacial area factor ξ^{lv} 80Constant ofproton conductivity vs. saturation k_{σ} 1 Sm^{-1} Cell current density j_{cell} 4×10^3 $A m^{-2}$ Relative humidity RH 0.8 Cathode pressure p_{cell} 1.5×10^5 Pa	Viscosity of liquid water	μ_w		Pa s
Vaporization interfacial area factor ξ^{lv} 80 Constant of proton conductivity vs. saturation k_{σ} 1 Sm ⁻¹ Cell current density j_{cell} 4×10^3 A m ⁻² Relative humidity RH 0.8 Cathode pressure p_{cell} 1.5×10^5 Pa	Elementary charge	e_0		
Constant of proton conductivity vs. saturation k_{σ} 1 Sm ⁻¹ Cell current density j_{cell} 4×10^3 A m ⁻² Relative humidity RH 0.8 Cathode pressure p_{cell} 1.5×10^5 Pa	Vaporization rate constant		1.38×10^{17}	$Pa^{-1} m^{-2} s^{-1}$
Cell current density $j_{\rm cell}$ 4×10^3 A m $^{-2}$ Relative humidity RH 0.8 Cathode pressure $p_{\rm cell}$ 1.5×10^5 Pa	Vaporization interfacial area factor	$\xi^{ ext{lv}}$	80	
Relative humidity RH 0.8 Cathode pressure p_{cell} 1.5 × 10 ⁵ Pa	Constant of proton conductivity vs. saturation	k_{σ}	1	Sm^{-1}
Relative humidity RH 0.8 Cathode pressure p_{cell} 1.5 × 10 ⁵ Pa	Cell current density	$j_{ m cell}$	4×10^3	$\mathrm{A}~\mathrm{m}^{-2}$
	Relative humidity	RH		
Proton conductivity σ_0 1 S m ⁻¹	Cathode pressure	p_{cell}	1.5×10^{5}	
	Proton conductivity	σ_0	1	$\mathrm{S}~\mathrm{m}^{-1}$

vary in quite a wide range, from 0.01 to 1.0 bar. The value of k_{pc} is determined by the PSD and the contact angle of pores in the CCL.

In this Section we consider the case of variable \bar{D}_{ox} and σ . First we look into the effect of k_{pc} on the low frequency limiting impedance Z_{lim} indicated by the small red circle in Fig. 4. As shown in Fig. 5, the relationship between k_{pc} and the static impedance is non-monotonic, exhibiting a minimum value. At very low k_{pc} values, the steep slope of retention curve is located at capillary pressures near $p_{c,0}$. However, the steady state operates away from this pressure, where the retention curve slope is close to zero. This regime corresponds to a plateau of the static impedance at k_{pc} from 0.01 to 0.1 bar. As k_{pc} increases, the capillary pressure range with a high retention curve slope gradually extends to the operating p_c range, inducing an inductive loop where Z_{lim} decreases with increasing k_{pc} . However, the increase in k_{pc} also reduces the steepness of the slope, resulting in a smaller inductive loop diameter. After reaching the minimum, further increase in k_{pc} results in the growth of the static impedance Z_{lim} . Taking into account that infinite k_{pc} corresponds to the absence of a liquid transient, Eq. 14, we conclude that rapid liquid transient effects reduce the low-frequency impedance, thereby improving the cathode performance. This result agrees with the analytical result for the CCL resistivity in Ref. [17].

In essence, given that the steady state operates within the capillary pressure range where k_{pc} has a significant impact, a higher k_{pc} indicates a reduced sensitivity of water saturation to variations in pressure, whereas a lower k_{pc} accentuates this sensitivity. Subsequently, we investigate the influence of the parameter k_{pc} on the size of the inductive loop.

Upon increasing k_{pc} from 0.7 bar to 1 bar, a consistent trend emerges, revealing a reduction in the size of the inductive loop. Consequently, lower values of k_{pc} correspond to larger inductive loops, underscoring the heightened susceptibility of liquid saturation to fluctuations in capillary pressure.

Does relaxation of liquid saturation reduce the cathode static resistivity?.—From Figs. 4a, 4b it follows that a pronounced relaxation of liquid saturation reduces the cathode low–frequency resistivity. Similar results have been reported by Kulikovsky¹⁷ who demonstrated analytically that the current–dependent proton conductivity σ causes a reduction of the static resistivity.

This also means that for $\omega \to 0$, the system reaches a pseudo steady state differing from the steady state obtained at a constant liquid saturation (cf. Figs. 4b and 4c). In every frame of Fig. 4, the system tends to a separate pseudo steady state determined by the perturbed transport parameters. At $\tilde{\omega} \to 0$, the exponent in Fourier–transforms, Eqs. D1, tends to unity and equations determining the impedance still contain the small-amplitude perturbation amplitudes of transport parameters. This distinguishes the problem from the pure static one.

However, theoretically, the perturbation amplitudes could be taken infinitesimally small and the perturbed system would differ from the pure static one by the presence of negligible terms. Paradoxically, in the limit of $\tilde{\omega} \to 0$, the system with negligible perturbations tends to the steady state which differs quite substantially from the "pure" static (unperturbed) state. This suggests that at least the "post–inductive" steady–state is unstable. Analysis of the system stability is performed in the next section.

Stability analysis.—To simplify analysis, we neglect water vaporization in the CCL. This condition can be achieved under sufficiently low cell temperature and current. The governing equations for this system are

$$\frac{1}{V_m}\frac{\partial s}{\partial t} + \nabla J_L = \frac{Q_{ORR}}{2F},\tag{18}$$

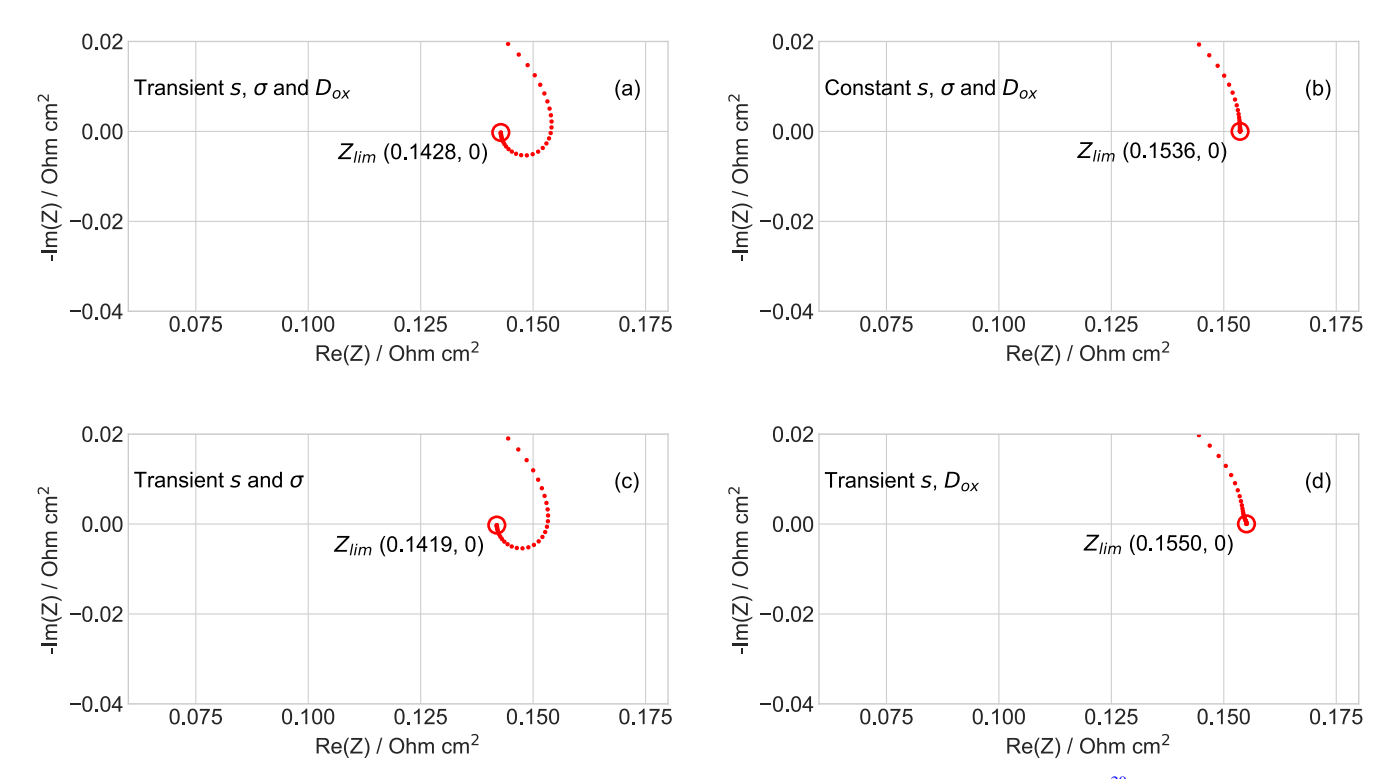


Figure 4. Zoomed Nyquist spectra of the electrochemical impedance, Eq. 17, for the water retention curve from Olbrich et al.²⁰ for cases of (a) transient s, σ , D_{ox} , (b) constant s, σ , D_{ox} , (c) transient s, σ and constant D_{ox} , (d) transient s, D_{ox} and constant σ .

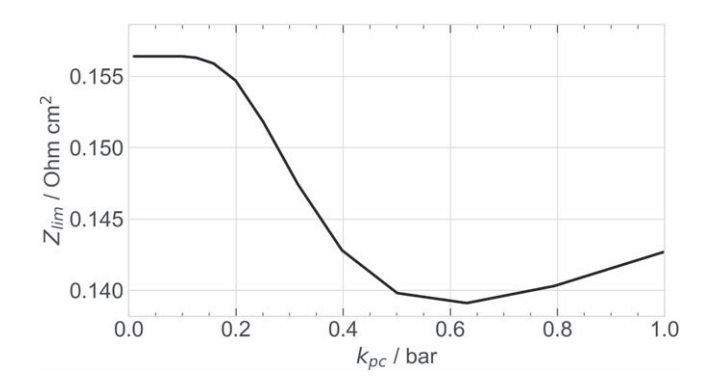


Figure 5. The relationship between the parameter k_{pc} determining the retention curve slope and the static impedance Z_{lim} .

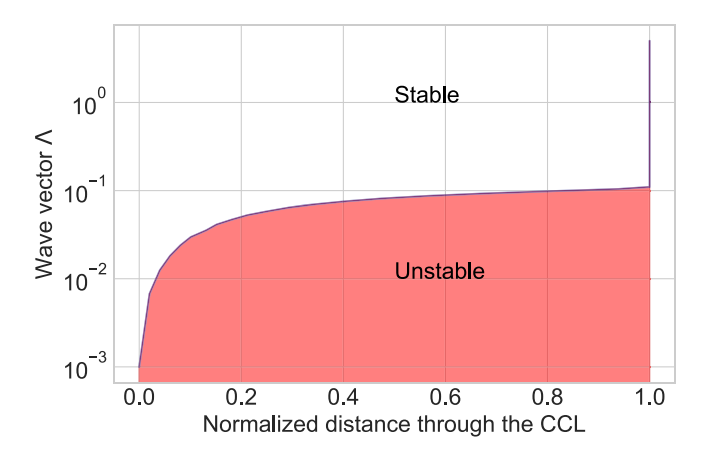


Figure 6. The stability diagram. The line where the imaginary part of Ω equates to zero, $\operatorname{Im}(\Omega)=0$, separates the stable and unstable regimes of CCL operation. Parameters are taken from Table I.

$$\frac{1}{RT}\frac{\partial p_{O_2}}{\partial t} + \nabla J_{O_2} = -\frac{Q_{ORR}}{4F},\tag{19}$$

$$C_{dl}\frac{\partial \eta}{\partial t} + \nabla J_p = -Q_{ORR}.$$
 [20]

We transform Eqs. 18–20 into dimensionless form (Appendix G), linearize the resulting equations and apply perturbations of the form

$$\tilde{y}(\tilde{x}, \tilde{t}) = \tilde{y}^0(\tilde{x}) + \tilde{y}^1(\Lambda, \Omega) \exp(i(\Lambda \tilde{x} - \Omega \tilde{t})), \quad |\tilde{y}^1| \ll \tilde{y}^0, \quad [21]$$

where \tilde{y} stands for \tilde{p}_L , $\tilde{\eta}$ and \tilde{p}_{O_2} .

Physically, the term in the exponential function in Eq. 21 means that the applied perturbation varies harmonically in time and space. The spatial $(\tilde{x}-)$ variation of the perturbation is described by the wave vector Λ , and the temporal variation is described by the frequency Ω , which is a complex–valued variable. Our goal is to derive and analyze the dispersion relation $\Omega(\Lambda)$. From Eqs. 21 it follows, that if for some Λ , the frequency Ω has a positive imaginary part, the system is unstable. Indeed, let $\Omega = \Omega_{re} + \mathrm{i} |\Omega_{im}|$; then $\exp(-\mathrm{i}\Omega\tilde{t}) = \exp(-\mathrm{i}\Omega_{re}\tilde{t})\exp(|\Omega_{im}|\tilde{t})$, meaning that the second factor on the right hand side is growing with time.

The mathematical details of the derivation of the $\Omega(\Lambda)$ equation are given in Appendix G. Numerical calculations of Ω are performed with parameters from Table I. Figure 6 displays the stability diagram of the system on the $(\Lambda, \operatorname{Im}(\Omega))$ plane. The line that separates the stable and the unstable domains corresponds to the solution of $\operatorname{Im}(\Omega)(\Lambda)=0$ (Fig. 6). Notably, within the range of Λ values spanning from 0.001 to 0.1, all scenarios consistently exhibit positive values of the imaginary part of Ω , indicating the presence of instability across this range of parameters.

The mechanism of instability is as follows. Small growth of the ORR overpotential increases the cell current and thereby leads to higher liquid saturation and liquid water pressure in the CCL. Higher saturation, in turn, retards oxygen transport and further increases the overpotential. This positive feedback loop could work until the CCL is fully flooded when p_L exceeds the critical value (tipping point).

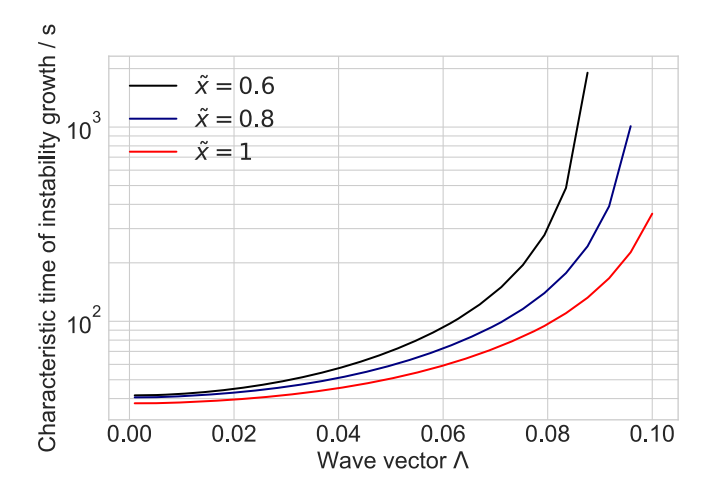


Figure 7. The characteristic time of instability growth vs wave vector Λ for the indicated distances from the membrane.

Calculations show that for $\tilde{k}_L=0$, the system is stable, signifying that the source of instability is the transient nature of liquid pressure. We conclude that the post–inductive steady states in Figs. 4a, 4c could be unreachable due to the instability discussed above. Figure 7 shows the characteristic time of instability growth as a function of wave vector Λ

In 2006, Nazarov and Promislow²⁷ reported instability of PEM fuel cell with respect to a small variation of the membrane humidification. Within the scope of their model, the instability occurs due to the following mechanism. A small local increase in water content of the membrane separating the anode and cathode leads to the local increase in membrane proton conductivity. The increase in conductivity in turn, increases the local current through the perturbed domain, which leads to growing water production in the adjacent domain of the CCL. If current in the external circuit is fixed, the cell splits up into two domains, with the small current in a water–deficient domain, and larger current in a water–filled domain.

The instability of the CCL discussed here works the other way round. It could eventually split up the cell into two domains: one with high liquid CCL saturation (flooded), where less oxygen is transported and less current is produced, and another with low saturation, where most of the current is generated. Possible candidates for such a split are the under–rib and under–channel domains with a lot of water and lower current in the first one, and less water, but higher current in the second one. ^{28,29}

Our analysis is linear and it only shows that the "post-inductive" steady-state is unstable. However, it tells nothing about the non-linear phase of instability development, which would require numerical calculations. We expect that the instability would lead to oscillating behavior of the cell potential and to the respective oscillations (perhaps, chaotic) of the cell low-frequency impedance.

In this work, we do not consider effects of liquid water transport in the GDL. Work on these effects is underway and the results will be published elsewhere. For simplicity, we also assume that D_{ν} is a constant parameter. The model in its present form is complicated and a number of simplifying assumptions helped us to solve it. The dependence of D_{ν} on liquid saturation will be incorporated in the next version of our model.

Finally, it should be noted that the EIS spectra are extremely sensitive to the shape of the WRC and to the cell operating parameters. The present paper aims at understanding the mechanism behind the formation of an inductive loop in the Nyquist spectrum. To this end, the cathode RH and the cell current density have been selected in order to get an inductive loop in two spectra the Fig. 3. However, our calculations show that small variations of the WRC shape, cathode RH, or cell current density could lead to dramatic changes in the shape of spectra: the

inductive loop may either disappear, or the capacitive oxygen–transport arc could form instead of the loop (see open circle curves in Figs. 2 and 3.). Experimental impedance spectra in the literature qualitatively agree with this behavior: some spectra exhibit inductive loops, while others do not.³⁰ The parametric dependence of impedance spectra is currently being studied with the model above. The results will be published elsewhere.

Conclusions

A model for the PEM fuel cell cathode impedance has been developed. The model takes into account liquid and gaseous water transport in the cathode catalyst layer and the dependence of oxygen and proton transport parameters on the dynamic liquid water saturation in the CCL. The slow relaxation of oxygen diffusivity yields a second capacitive semicircle which increases the static resistivity. In contrast, the slow relaxation of proton conductivity upon variation of liquid water content produces an inductive loop in the Nyquist spectrum.

A key aspect in the formation of the inductive loop is the dependence of the liquid saturation on the capillary pressure in the CCL. In the range of capillary pressurewhere the saturation does not depend on it, the inductive loop does not form. A stability analysis of the linearized reduced system of equations shows that the steady state corresponding to the inductive loop is unstable with respect to spatial fluctuations. A small local increase in overpotential leads to local growth of the liquid saturation. This increase lowers the rate of oxygen transport, which further increases the overpotential. This positive feedback loop may work until the catalyst layer is completely flooded. The characteristic time of instability growth varies from 30 s up to several hundred seconds, depending on the spatial location and size of the fluctuation. This type of instability could cause a spatial splitting of the CCL into domains with high and low water content, with the current production mainly in the non-flooded domain. Detailed analysis of this effect will require solution of the two-dimensional extension of the current model in time domain.

Appendix A. The Detailed Governing equations for Water, Oxygen and Proton Transport in CCL

To simplify calculations, we introduce two parameters

$$k_L = \frac{K_L}{\mu V_{vv}}, \quad k_{lv} = \frac{e_0 \kappa \xi^{lv}}{F l_t}.$$
 [A1]

Substituting J_L , Q_{ORR} , Q_{lv} from Eqs. 6, 11, 12 into 1, we get

$$\frac{1}{V_m}\frac{\partial s}{\partial t} - k_L \frac{\partial^2 p_L}{\partial x^2} = \frac{i_*}{2F} \left(\frac{p_{O_2}}{p_{O_2}^{ref}}\right) \exp\left(\frac{\eta}{b}\right) - k_{lv}(p_v^s - p_v). \quad [A2]$$

Substituting J_{ν} , Q_{ORR} , $Q_{l\nu}$ from Eqs. 7, 11, 12 into 2 gives

$$\frac{1}{RT}\frac{\partial p_{\nu}}{\partial t} - \frac{D_{\nu}}{RT}\frac{\partial^{2} p_{\nu}}{\partial x^{2}} = k_{l\nu}(p_{\nu}^{s} - p_{\nu})$$
 [A3]

Substituting J_{O2} , Q_{ORR} from Eqs. 8, 11 into 3 leads to

$$\frac{\partial p_{O_2}}{\partial t} - \frac{\partial}{\partial x} \left(D_{ox} \frac{\partial p_{O_2}}{\partial x} \right) = -\frac{RTi_*}{4F} \left(\frac{p_{O_2}}{p_{O_2}^{ref}} \right) \exp\left(\frac{\eta}{b} \right), \quad [A4]$$

and substitution of J_p , Q_{ORR} from Eqs. 10, 11, into Eq. 4 yields

$$C_{dl} \frac{\partial \eta}{\partial t} - \frac{\partial}{\partial x} \left(\sigma \frac{\partial \eta}{\partial x} \right) = -i_* \left(\frac{p_{O_2}}{p_{O_2}^{ref}} \right) \exp\left(\frac{\eta}{b} \right).$$
 [A5]

Finally, substitution of J_h from Eq. 9 into Eq. 5 results in

$$\frac{\partial p_b}{\partial t} - D_b \frac{\partial^2 p_b}{\partial x^2} = 0.$$
 [A6]

Appendix B. The Dimensionless Governing equations for Water, Oxygen, Proton Transport in CCL

To simplify calculations, we introduce dimensionless variables:

$$\tilde{x} = \frac{x}{l_{t}}, \quad \tilde{t} = \frac{t}{t_{*}}, \quad \tilde{D}_{ox} = \frac{4Fp_{O_{2}}^{ref}D_{ox}}{\sigma_{*}bRT},$$

$$\tilde{D}_{b} = \frac{4Fp_{O_{2}}^{ref}D_{b}}{\sigma_{*}bRT}, \quad \tilde{D}_{v} = \frac{4Fp_{O_{2}}^{ref}D_{v}}{\sigma_{*}bRT},$$

$$\tilde{k}_{L} = \frac{4Fp_{O_{2}}^{ref}k_{L}}{i_{*}l_{t}^{2}}, \quad \tilde{k}_{lv} = \frac{4Fp_{O_{2}}^{ref}k_{lv}}{i_{*}}, \quad \tilde{p}_{v} = \frac{p_{v}}{p_{O_{2}}^{ref}},$$

$$\tilde{p}_{L} = \frac{p_{L}}{p_{O_{2}}^{ref}}, \quad \tilde{p}_{b} = \frac{p_{b}}{p_{O_{2}}^{ref}}, \quad \tilde{p}_{O_{2}} = \frac{p_{O_{2}}}{p_{O_{2}}^{ref}},$$

$$\tilde{\sigma} = \frac{\sigma}{\sigma_{*}}, \quad \tilde{\eta} = \frac{\eta}{b}, \quad \tilde{j} = \frac{j}{j_{*}},$$

$$\tilde{\omega} = \omega t_{*}, \quad j_{*} = \frac{\sigma_{*}b}{l_{*}}, \quad t_{*} = \frac{C_{dl}b}{i_{*}},$$
[B1]

where x is the coordinate thorough the cell, l_t the thickness of CCL, t time, t_* the characteristic time, D_{ox} the oxygen diffusivity of CCL, $p_{O_2}^{ref}$ the reference oxygen pressure D_b the oxygen diffusivity of GDL, F Faraday constant, σ proton conductivity of CCL, σ_* proton conductivity of CCL at zero current density, b ORR Tafel slope, D_v the water vapor diffusivity, p_v^s saturated water vapor pressure, p_L^{ref} reference (inlet) liquid water pressure, η ORR overpotential (positive by convention), j local proton current density in the CCL, j_* characteristic current density, i_* ORR volumetric exchange current density, ω angular frequency of the applied AC signal, and C_{all} double layer capacitance. The saturated water vapor pressure p_v^s (bar) is calculated using the standard cubic dependence on temperature T (K):

$$\begin{split} \log_{10}(p_v^s) &= -2.1794 + 0.029\ 53 \cdot (T-273) - 9.1837 \cdot 10^{-5} \cdot (T-273)^2 \\ &+ 1.4454 \cdot 10^{-7} \cdot (T-273)^3 \end{split}$$
 [B2]

Using dimensionless variables, Eqs. A2-A6 transform to

$$\gamma^2 \frac{\partial s}{\partial \tilde{t}} - \tilde{k}_L \frac{\partial^2 \tilde{p}_L}{\partial \tilde{x}^2} = 2\tilde{p}_{O_2} \exp(\tilde{\eta}) - \tilde{k}_{lv} (\tilde{p}_v^s - \tilde{p}_v),$$
 [B3]

$$\mu^2 \frac{\partial \tilde{p}_{\nu}}{\partial \tilde{t}} - \varepsilon^2 \tilde{D}_{\nu} \frac{\partial^2 \tilde{p}_{\nu}}{\partial \tilde{x}^2} = \tilde{k}_{l\nu} (\tilde{p}_{\nu}^s - \tilde{p}_{\nu}),$$
 [B4]

$$\mu^2 \frac{\partial \tilde{p}_{O_2}}{\partial \tilde{t}} - \varepsilon^2 \frac{\partial}{\partial \tilde{x}} \left(\tilde{D}_{ox} \frac{\partial \tilde{p}_{O_2}}{\partial \tilde{x}} \right) = -\tilde{p}_{O_2} \exp(\tilde{\eta}).$$
 [B5]

$$\frac{\partial \tilde{\eta}}{\partial \tilde{t}} - \varepsilon^2 \frac{\partial}{\partial \tilde{x}} \left(\tilde{\sigma} \frac{\partial \tilde{\eta}}{\partial \tilde{x}} \right) = -\tilde{p}_{O_2} \exp(\tilde{\eta}).$$
 [B6]

$$\mu^2 \frac{\partial \tilde{p}_b}{\partial \tilde{t}} - \varepsilon^2 \tilde{D}_b \frac{\partial^2 \tilde{p}_b}{\partial \tilde{x}^2} = 0,$$
 [B7]

where

$$\gamma = \sqrt{\frac{4F}{V_m C_{dl} b}}, \quad \varepsilon = \sqrt{\frac{\sigma_* b}{i_* l_*^2}}, \quad \mu = \sqrt{\frac{4F p_{O_2}^{ref}}{C_{dl} b R T}}.$$
[B8]

Appendix C. Steady State Dimensionless Equations

In steady state, Eq. B6 transforms to

$$\varepsilon^{2} \frac{\partial}{\partial \tilde{x}} \left(\tilde{\sigma}^{0} \frac{\partial \tilde{\eta}^{0}}{\partial \tilde{x}} \right) = \tilde{p}_{O_{2}}^{0} e^{\tilde{\eta}^{0}}, \quad \frac{\partial \tilde{\eta}^{0}}{\partial \tilde{x}} \Big|_{\tilde{x}=0} = -\frac{\tilde{J}_{cell}}{\tilde{\sigma}^{0}}, \quad \frac{\partial \tilde{\eta}^{0}}{\partial \tilde{x}} \Big|_{\tilde{x}=1} = 0,$$
[C1]

where the left boundary condition stems from he Ohm's law, and the right b.c. means zero proton current density through the CCL/GDL interface. Equation B3 transforms to

$$-\tilde{k}_{L} \frac{\partial^{2} \tilde{p}_{L}^{0}}{\partial \tilde{x}^{2}} = 2\tilde{p}_{O_{2}}^{0} e^{\tilde{\eta}^{0}} - \tilde{k}_{lv} (\tilde{p}_{v}^{s} - \tilde{p}_{v}^{0}),$$

$$\frac{\partial \tilde{p}_{L}^{0}}{\partial \tilde{x}} \bigg|_{\tilde{x}=0} = 0, \quad \tilde{p}_{L}^{0}(1) = \tilde{p}_{cell}, \quad [C2]$$

Here, the left b.c. means zero liquid water flux in the membrane, one of the model assumptions. Th right b.c. expresses zero capillary pressure at the CCL/GDL interface, which is quite reasonable taking into account large GDL pore radii. Equation B4 transforms to

$$-\varepsilon^2 \tilde{D}_v \frac{\partial^2 \tilde{p}_v^0}{\partial \tilde{x}^2} = \tilde{k}_{lv} (\tilde{p}_v^s - \tilde{p}_v^0), \quad \frac{\partial \tilde{p}_v^0}{\partial \tilde{x}} \bigg|_{\tilde{x}=0} = 0, \quad \tilde{p}_v^0(1) = \tilde{p}_v^s.$$
[C3]

where the left b.c. means zero water vapor flux through the membrane, and the right b.c. stems from continuity of the water vapor concentration at the CCL/GDL interface. Equation B5 takes the form

$$\begin{split} \varepsilon^2 \frac{\partial}{\partial \tilde{x}} \left(\tilde{D}_{ox}^0 \frac{\partial \tilde{p}_{O_2}^0}{\partial \tilde{x}} \right) \\ = & \tilde{p}_{O_2}^0 e^{\tilde{\eta}^0}, \quad \frac{\partial \tilde{p}_{O_2}^0}{\partial \tilde{x}} \bigg|_{\tilde{x}=0} = 0, \quad \tilde{p}_{O_2}^0(1) = \tilde{p}_b^0(1), \end{split}$$
 [C4]

with the zero oxygen flux in the membrane and continuity of the oxygen concentration at the CCL/GDL interface as the left and right b.c., respectively.

In the steady state, Eq. B7 transforms to

$$\varepsilon^{2} \tilde{D}_{b} \frac{\partial^{2} \tilde{p}_{b}^{0}}{\partial \tilde{x}^{2}} = 0, \quad \tilde{D}_{ox}^{0} \frac{\partial \tilde{p}_{O_{2}}^{0}}{\partial \tilde{x}} \bigg|_{\tilde{x}=1-} = \tilde{D}_{b}^{0} \frac{\partial \tilde{p}_{b}^{0}}{\partial \tilde{x}} \bigg|_{\tilde{x}=1+},$$

$$\tilde{p}_{b}^{0} (1 + \tilde{l}_{b}) = 1, \quad [C5]$$

where the b.c. mean continuity of the oxygen flux at the CCL/GDL interface, and fixed oxygen concentration in the cathode channel. Here, l_b is the GDL thickness.

Adopting the fitting function for water retention curve in Eq. 14, we have

$$s^{0} = a + \frac{(1-a)}{2} \left(1 + \tanh\left(\frac{p_{c}^{0} - p_{c,0}}{k_{pc}}\right) \right)$$

$$\tilde{D}_{ox}^{0} = (1-s^{0})^{2} \tilde{D}_{ox,d}^{0},$$

$$\tilde{\sigma}^{0} = \tilde{k}_{\sigma} s^{0},$$

where $\tilde{k}_{\sigma} = k_{\sigma}/\sigma_*$. We neglect the influence of s on \tilde{D}_{v} and \tilde{k}_{L} .

Appendix D. Transient State

To perform linearization and Fourier-transform of Eqs. B3, B4 and B5, we use the following expansions

$$y(\tilde{x}, \tilde{t}) = y^0(\tilde{x}) + y^1(\tilde{x}, \tilde{\omega}) \exp(i\tilde{\omega}\tilde{t}), \quad |y^1| \ll y^0,$$
 [D1]

where y stands for s, \tilde{p}_L , \tilde{p}_v , \tilde{p}_{O_2} , \tilde{p}_b , $\tilde{\eta}$, and the superscripts 0, 1 mark the static value and the small perturbation amplitude, respectively.

Substituting s, \tilde{p}_L , \tilde{p}_{O_2} , \tilde{p}_{ν} , Eqs. D1, into B3–B6, and subtracting the respective static equation, we obtain

$$\tilde{k}_{L} \frac{\partial^{2} \tilde{p}_{L}^{1}}{\partial \tilde{x}^{2}} = \gamma^{2} i \tilde{\omega} s^{1} - 2 e^{\tilde{\eta}^{0}} \tilde{p}_{O_{2}}^{1} - 2 \tilde{p}_{O_{2}}^{0} e^{\tilde{\eta}^{0}} \tilde{\eta}^{1} - \tilde{k}_{lv} \tilde{p}_{v}^{1},$$
 [D2]

$$\varepsilon^2 \tilde{D}_{\nu}^0 \frac{\partial^2 \tilde{p}_{\nu}^1}{\partial \tilde{x}^2} = (i\tilde{\omega}\mu^2 + \tilde{k}_{l\nu})\tilde{p}_{\nu}^1,$$
 [D3]

$$\begin{split} \varepsilon^2 \frac{\partial}{\partial \tilde{x}} \left(\tilde{D}_{ox}^0 \frac{\partial \tilde{p}_{O_2}^1}{\partial \tilde{x}} \right) \\ = & (\mathrm{i} \tilde{\omega} \mu^2 + \mathrm{e}^{\tilde{\eta}^0}) \tilde{p}_{O_2}^1 + \tilde{p}_{O_2}^0 \, \mathrm{e}^{\tilde{\eta}^0} \tilde{\eta}^1 - \varepsilon^2 \frac{\partial}{\partial \tilde{x}} \left(\tilde{D}_{ox}^1 \frac{\partial \tilde{p}_{O_2}^0}{\partial \tilde{x}} \right), \end{split} \quad [D4]$$

$$\varepsilon^{2} \frac{\partial}{\partial \tilde{x}} \left(\tilde{\sigma}^{0} \frac{\partial \tilde{\eta}^{1}}{\partial \tilde{x}} \right) = e^{\tilde{\eta}^{0}} \tilde{p}_{O_{2}}^{1} + (\tilde{p}_{O_{2}}^{0} e^{\tilde{\eta}^{0}} + i\tilde{\omega}) \tilde{\eta}^{1} - \varepsilon^{2} \frac{\partial}{\partial \tilde{x}} \left(\tilde{\sigma}^{1} \frac{\partial \tilde{\eta}^{0}}{\partial \tilde{x}} \right).$$
[D5]

The boundary conditions to close Eqs. D2-D5 are

$$\frac{\partial \tilde{p}_L^1}{\partial \tilde{x}} \bigg|_{\tilde{x}=0} = 0, \quad \tilde{p}_L^1(1) = 0, \quad [D6]$$

$$\left. \frac{\partial \tilde{p}_{\nu}^{1}}{\partial \tilde{x}} \right|_{\tilde{z}=0} = 0, \quad \tilde{p}_{\nu}^{1}(1) = 0, \quad [D7]$$

$$\frac{\partial \tilde{p}_{O_2}^1}{\partial \tilde{x}} \bigg|_{\tilde{x}=0} = 0, \quad \tilde{p}_{O_2}^1(1) = \tilde{p}_b^1(1), \quad [D8]$$

$$\tilde{\eta}^1|_{\tilde{x}=1} = \tilde{\eta}_{perturb}, \quad \frac{\partial \tilde{\eta}^1}{\partial \tilde{x}} \bigg|_{\tilde{x}=1} = 0.$$
 [D9]

Adopting the fitting function for water retention curve in Eq. 14, we have

$$s^{1} = \frac{(1-a)}{2} \left(1 - \tanh^{2} \left(\frac{p_{c}^{0} - p_{c,0}}{k_{pc}} \right) \right) \frac{(\tilde{p}_{L}^{1} - \tilde{p}_{v}^{1} - \tilde{p}_{O_{2}}^{1}) p_{O_{2}}^{ref}}{k_{pc}}$$

$$\tilde{\sigma}^1 = \tilde{k}_{\sigma} s^1,$$
 [D10]

$$\tilde{D}_{ox}^{1} = -2(1 - s^{0})s^{1}\tilde{D}_{ox,d}^{0}.$$
 [D11]

We neglect the influence of saturation on \tilde{D}_{ν} and \tilde{k}_{L} , thus $\tilde{D}_{\nu}^{1} = 0$ and $\tilde{k}_{L}^{1} = 0$.

Appendix E. The Solution to $\tilde{p}_b^1(1)$

Substituting \tilde{p}_b in Eq. B7 with Eq. D1 and subtracting the static equation, we obtain

$$\mu^2 \tilde{p}_b^1 i \tilde{\omega} - \varepsilon^2 \tilde{D}_b^0 \frac{\partial^2 \tilde{p}_b^1}{\partial \tilde{x}^2} = 0$$
 [E1]

The boundary conditions are

$$\tilde{D}_{ox}^{0} \frac{\partial \tilde{p}_{O_{2}}^{1}}{\partial \tilde{x}} \bigg|_{\tilde{x}=1} = \tilde{D}_{b}^{0} \frac{\partial \tilde{p}_{b}^{1}}{\partial \tilde{x}} \bigg|_{\tilde{x}=1}, \quad \tilde{p}_{b}^{1} (1 + \tilde{l}_{b}) = \tilde{p}_{h}^{1}$$
 [E2]

The solution for $\tilde{p}(\tilde{x})$ is

$$\tilde{p}_b^1 = \frac{A}{N} \cosh(\phi \tilde{x}) - \frac{B}{N} \sinh(\phi \tilde{x}), \quad [E3]$$

where

$$A = \sinh(\phi(1+\tilde{l}_b)) \frac{\tilde{D}_{ox}^0}{\tilde{D}_b^0 \phi} \frac{\partial \tilde{p}_{O_2}^1}{\partial \tilde{x}} \bigg|_{\tilde{x}=1} - \cosh(\phi) \tilde{p}_h^1, \qquad [E4]$$

$$B = \cosh\left(\phi(1+\tilde{l}_b)\right) \frac{\tilde{D}_{ox}^0}{\tilde{D}_b^0 \phi} \frac{\partial \tilde{p}_{O_2}^1}{\partial \tilde{x}} \bigg|_{\tilde{x}=1} - \sinh\left(\phi\right) \tilde{p}_h^1, \quad [E5]$$

and

$$N = \sinh(\phi)\sinh(\phi(1+\tilde{l}_b)) - \cosh(\phi(1+\tilde{l}_b))\cosh(\phi). \quad [E6]$$

Thus,

$$\tilde{p}_b^1(1) = -\alpha \tilde{D}_{ox}^0 \frac{\partial \tilde{p}_{O_2}^1}{\partial \tilde{x}} \bigg|_{\tilde{x}=1} + \beta \tilde{p}_h^1$$
 [E7]

where

$$\alpha = \frac{\tanh(\tilde{l}_b \phi)}{\tilde{D}_b^0 \phi}, \quad \beta = \frac{1}{\cosh(\tilde{l}_b \phi)}, \quad \phi = \mu \sqrt{\frac{i\tilde{\omega}}{\varepsilon^2 \tilde{D}_b^0}}.$$
 [E8]

Appendix F. Appendix F. Limiting Cases

For the limiting case 1, with $s^1 = 0$, $D^1 = 0$, $\sigma^1 = 0$, $\tilde{D}_{\nu}^1 = 0$, Eqs. D2–D5 reduce to

$$\tilde{k}_L \frac{\partial^2 \tilde{p}_L^1}{\partial \tilde{x}^2} = -2\tilde{p}_{O_2}^1 e^{\tilde{\eta}^0} - 2\tilde{p}_{O_2}^0 e^{\tilde{\eta}^0} \tilde{\eta}^1 - \tilde{k}_{lv} \tilde{p}_v^1,$$
 [F1]

$$\varepsilon^2 \tilde{D}_{\nu}^0 \frac{\partial^2 \tilde{p}_{\nu}^1}{\partial \tilde{x}^2} = (i\tilde{\omega}\mu^2 + \tilde{k}_{l\nu})\tilde{p}_{\nu}^1,$$
 [F2]

$$\varepsilon^2 \frac{\partial}{\partial \tilde{x}} \left(\tilde{D}_{0x}^0 \frac{\partial^2 \tilde{p}_{O_2}^1}{\partial \tilde{x}^2} \right) = \tilde{p}_{O_2}^1 \left(i\tilde{\omega}\mu^2 + e^{\tilde{\eta}^0} \right) + \tilde{p}_{O_2}^0 e^{\tilde{\eta}^0} \tilde{\eta}^1,$$
 [F3]

$$\varepsilon^2 \frac{\partial}{\partial \tilde{x}} \left(\tilde{\sigma}^0 \frac{\partial^2 \tilde{\eta}^1}{\partial \tilde{x}^2} \right) = \tilde{p}_{O_2}^1 e^{\tilde{\eta}^0} + (\tilde{p}_{O_2}^0 e^{\tilde{\eta}^0} + i\tilde{\omega}) \tilde{\eta}^1.$$
 [F4]

For the limiting case 2, when $D_{ox}^1 = 0$, Eqs. D2–D5 reduce to

$$\tilde{k}_{L} \frac{\partial^{2} \tilde{p}_{L}^{1}}{\partial \tilde{x}^{2}} = \gamma^{2} i \tilde{\omega} s^{1} - 2 e^{\tilde{\eta}^{0}} \tilde{p}_{O_{2}}^{1} - 2 \tilde{p}_{O_{2}}^{0} e^{\tilde{\eta}^{0}} \tilde{\eta}^{1} - \tilde{k}_{lv} \tilde{p}_{v}^{1},$$
 [F5]

$$\varepsilon^2 \tilde{D}_{\nu}^0 \frac{\partial^2 \tilde{p}_{\nu}^1}{\partial \tilde{x}^2} = (i\tilde{\omega}\mu^2 + \tilde{k}_{l\nu})\tilde{p}_{\nu}^1,$$
 [F6]

$$\varepsilon^2 \frac{\partial}{\partial \tilde{x}} \left(\tilde{D}_{0x}^0 \frac{\partial \tilde{p}_{O_2}^1}{\partial \tilde{x}} \right) = (i\tilde{\omega}\mu^2 + e^{\tilde{\eta}^0}) \tilde{p}_{O_2}^1 + \tilde{p}_{O_2}^0 e^{\tilde{\eta}^0} \tilde{\eta}^1,$$
 [F7]

$$\varepsilon^{2} \frac{\partial}{\partial \tilde{x}} \left(\tilde{\sigma}^{0} \frac{\partial \tilde{\eta}^{1}}{\partial \tilde{x}} \right) = e^{\tilde{\eta}^{0}} \tilde{p}_{O_{2}}^{1} + (\tilde{p}_{O_{2}}^{0} e^{\tilde{\eta}^{0}} + i\tilde{\omega}) \tilde{\eta}^{1} - \varepsilon^{2} \frac{\partial}{\partial \tilde{x}} \left(\tilde{\sigma}^{1} \frac{\partial \tilde{\eta}^{0}}{\partial \tilde{x}} \right).$$
 [F8]

For the limiting case 3, when $\sigma^1 = 0$, Eqs. D2–D5 reduce to

$$\tilde{k}_{L} \frac{\partial^{2} \tilde{p}_{L}^{1}}{\partial \tilde{r}^{2}} = \gamma^{2} i \tilde{\omega} s^{1} - 2 e^{\tilde{\eta}^{0}} \tilde{p}_{O_{2}}^{1} - 2 \tilde{p}_{O_{2}}^{0} e^{\tilde{\eta}^{0}} \tilde{\eta}^{1} - \tilde{k}_{lv} \tilde{p}_{v}^{1},$$
 [F9]

$$\varepsilon^2 \tilde{D}_v^0 \frac{\partial^2 \tilde{p}_v^1}{\partial \tilde{x}^2} = (i\tilde{\omega}\mu^2 + \tilde{k}_{lv})\tilde{p}_v^1,$$
 [F10]

$$\begin{split} \varepsilon^2 \frac{\partial}{\partial \tilde{x}} \left(\tilde{D}_{ox}^0 \frac{\partial \tilde{p}_{O_2}^1}{\partial \tilde{x}} \right) \\ &= (\mathrm{i} \tilde{\omega} \mu^2 + \mathrm{e}^{\tilde{\eta}^0}) \tilde{p}_{O_2}^1 + \tilde{p}_{O_2}^0 \, \mathrm{e}^{\tilde{\eta}^0} \tilde{\eta}^1 - \varepsilon^2 \frac{\partial}{\partial \tilde{x}} \left(\tilde{D}_{ox}^1 \frac{\partial \tilde{p}_{O_2}^0}{\partial \tilde{x}} \right), \end{split} \quad [F11]$$

$$\varepsilon^2 \frac{\partial}{\partial \tilde{x}} \left(\tilde{\sigma}^0 \frac{\partial \tilde{\eta}^1}{\partial \tilde{x}} \right) = e^{\tilde{\eta}^0} \tilde{p}_{O_2}^1 + (\tilde{p}_{O_2}^0 e^{\tilde{\eta}^0} + i\tilde{\omega}) \tilde{\eta}^1.$$
 [F12]

Appendix G. Appendix G. Stability Analysis of the Reduced

To simplify calculations, we use the dimensionless variables in Appendix B. Equations 18, 20, and 3 transform to

$$\gamma^2 \frac{\partial s}{\partial \tilde{t}} - \tilde{k}_L \frac{\partial^2 \tilde{p}_L}{\partial \tilde{x}^2} = 2\tilde{p}_{O_2} \exp(\tilde{\eta}),$$
 [G1]

$$\frac{\partial \tilde{\eta}}{\partial \tilde{t}} - \varepsilon^2 \frac{\partial}{\partial \tilde{x}} \left(\tilde{\sigma} \frac{\partial \tilde{\eta}}{\partial \tilde{x}} \right) = -\tilde{p}_{O_2} \exp(\tilde{\eta}), \quad [G2]$$

$$\mu^{2} \frac{\partial \tilde{p}_{O_{2}}}{\partial \tilde{t}} - \varepsilon^{2} \frac{\partial}{\partial \tilde{x}} \left(\tilde{D}_{ox} \frac{\partial \tilde{p}_{O_{2}}}{\partial \tilde{x}} \right) = -\tilde{p}_{O_{2}} \exp(\tilde{\eta}).$$
 [G3]

For the dependence of saturation on capillary pressure, a linear relation is adopted. The linear relation approximates the transition region in the Eq. 14 function in the range of capillary pressures $p_{c,0} - k_{pc} \le p_c \le p_{c,0} + k_{pc}$. Since vaporization is neglected, the vapor pressure remains constant and we can write

$$s = \frac{p_L - p_{O_2}}{k_{nc}} + s_0 - s_g,$$
 [G4]

where $s_g = (p_v + p_{N_2})/k_{pc}$. When $s_0 = s_g$, we have

$$s = \frac{p_L - p_{O_2}}{k_{pc}},$$
 [G5]

or, in the dimensionless form

$$s = k_{O_2}(\tilde{p}_L - \tilde{p}_{O_2}),$$
 [G6]

where $k_{O_2} = p_{O_2}^{ref}/k_{pc}$.

For proton conductivity σ in the CCL, we adopt Eq. 15, hence $\tilde{\sigma} = k_{\sigma} s / \sigma_*$, or

$$\tilde{\sigma} = \frac{k_{\sigma}k_{O_2}}{\sigma_{\omega}}(\tilde{p}_L - \tilde{p}_{O_2}). \tag{G7}$$

Given $k_{\sigma}/\sigma_* = 1$, we have $\tilde{\sigma} = k_{O_2}(\tilde{p}_L - \tilde{p}_{O_2})$.

For oxygen diffusivity D_{ox} in the CCL,

$$\tilde{D}_{ox} = (1 - k_{O_2}(\tilde{p}_L - \tilde{p}_{O_2}))^2 \tilde{D}_{ox,d}$$
 [G8]

With Eqs. G6, G7 and G8, G1, G2 and G3 are transformed to

$$\gamma^2 \frac{\partial (k_{O_2}(\tilde{p}_L - \tilde{p}_{O_2}))}{\partial \tilde{t}} - \tilde{k}_L \frac{\partial^2 \tilde{p}_L}{\partial \tilde{x}^2} = 2\tilde{p}_{O_2} \exp(\tilde{\eta}),$$
 [G9]

$$\frac{\partial \tilde{\eta}}{\partial \tilde{t}} - \varepsilon^2 \frac{\partial}{\partial \tilde{x}} \left(k_{O_2} (\tilde{p}_L - \tilde{p}_{O_2}) \frac{\partial \tilde{\eta}}{\partial \tilde{x}} \right) = -\tilde{p}_{O_2} \exp(\tilde{\eta}), \quad [G10]$$

$$\begin{split} &\mu^2 \frac{\partial \tilde{p}_{O_2}}{\partial \tilde{t}} - \varepsilon^2 \tilde{D}_{ox,d} \frac{\partial}{\partial \tilde{x}} \Biggl((1 - k_{O_2} (\tilde{p}_L - \tilde{p}_{O_2}))^2 \frac{\partial \tilde{p}_{O_2}}{\partial \tilde{x}} \Biggr) \\ = &- \tilde{p}_{O_2} \exp(\tilde{\eta}). \end{split} \tag{G11}$$

Now, we introduce perturbations to the system, a time-dependent perturbation with complex–valued frequency Ω , and an x-dependent perturbation with the real positive wave vector Λ . To perform linearizaton and Fourier-transform of Eqs. G9, G10 and G11, we use the expansions 21.

Substituting Eqs. 21 into G9, G10 and G11, and subtracting the respective static equation, we obtain a system of linear equations for the perturbation amplitudes \tilde{p}_L^1 , $\tilde{\eta}^1$ and $\tilde{p}_{O_2}^1$:

$$\begin{pmatrix} a_{11} - i\Omega\gamma^2 k_{O_2} & a_{12} & a_{13} + i\Omega\gamma^2 k_{O_2} \\ a_{21} & a_{22} - i\Omega & a_{23} \\ a_{31} & a_{32} & a_{33} - i\Omega\mu^2 \end{pmatrix} \begin{pmatrix} \tilde{p}_L^1 \\ \tilde{\eta}^1 \\ \tilde{p}_{O_2}^1 \end{pmatrix} = \begin{pmatrix} 0 \\ 0 \\ 0 \end{pmatrix} \quad [G12]$$

where the matrix elements are

$$a_{11} = \tilde{k}_L \Lambda^2,$$

 $a_{12} = -2\tilde{p}_{O_2}^0 e^{\tilde{\eta}^0},$
 $a_{13} = -2e^{\tilde{\eta}^0},$ [G13]

$$\begin{aligned} a_{21} &= -\varepsilon^2 k_{O_2} \bigg(\mathrm{i} \Lambda \frac{\partial \tilde{\eta}^0}{\partial \tilde{x}} + \frac{\partial^2 \tilde{\eta}^0}{\partial \tilde{x}^2} \bigg), \\ a_{22} &= \tilde{p}_{O_2}^0 \, \mathrm{e}^{\tilde{\eta}^0} \\ &- \varepsilon^2 k_{O_2} \bigg(\mathrm{i} \Lambda \frac{\partial (\tilde{p}_L^0 - \tilde{p}_{O_2}^0)}{\partial \tilde{x}} - (\tilde{p}_L^0 - \tilde{p}_{O_2}^0) \Lambda^2 \bigg), \\ a_{23} &= \varepsilon^2 k_{O_2} \bigg(\mathrm{i} \Lambda \frac{\partial \tilde{\eta}^0}{\partial \tilde{x}} + \frac{\partial^2 \tilde{\eta}^0}{\partial \tilde{x}^2} \bigg) + \mathrm{e}^{\tilde{\eta}^0}, \end{aligned} \qquad [G14]$$

$$a_{31} &= 2k_{O_2} \varepsilon^2 \tilde{D}_{Ox,d} \bigg(-k_{O_2} \frac{\partial (\tilde{p}_L^0 - \tilde{p}_{O_2}^0)}{\partial \tilde{x}} \frac{\partial \tilde{p}_{O_2}^0}{\partial \tilde{x}} + \mathrm{i} \Lambda \bigg) \bigg),$$

$$a_{32} &= \tilde{p}_{O_2}^0 \, \mathrm{e}^{\tilde{\eta}^0},$$

$$a_{33} &= \varepsilon^2 \tilde{D}_{Ox,d} \bigg) \bigg(\frac{\partial^2 \tilde{p}_{O_2}^0}{\partial \tilde{x}} + \mathrm{i} \Lambda \bigg) \bigg),$$

$$+ \Lambda^2 (1 - k_{O_2} (\tilde{p}_L^0 - \tilde{p}_{O_2}^0)) \frac{\partial (\tilde{p}_L^0 - \tilde{p}_{O_2}^0)}{\partial \tilde{x}} \bigg) + \lambda^2 (1 - k_{O_2} (\tilde{p}_L^0 - \tilde{p}_{O_2}^0))^2 \bigg) \bigg(\frac{\partial \tilde{p}_{O_2}^0}{\partial \tilde{x}} - 2k_{O_2} (1 - k_{O_2} (\tilde{p}_L^0 - \tilde{p}_{O_2}^0)) + \tilde{p}_{O_2}^0 \bigg) \bigg) \bigg) \bigg(\frac{\partial \tilde{p}_{O_2}^0}{\partial \tilde{x}} + \mathrm{i} \Lambda \bigg) \bigg(\frac{\partial^2 \tilde{p}_{O_2}^0}{\partial \tilde{x}} + \mathrm{i} \Lambda \bigg) \bigg(\frac{\partial \tilde{p}_{O_2}^0}{\partial \tilde{x}} \bigg) \bigg) \bigg(\frac{\partial^2 \tilde{p}_{O_2}^0}{\partial \tilde{x}} + \mathrm{i} \Lambda \bigg) \bigg(\frac{\partial \tilde{p}$$

Nontrivial solutions to Eq. G12 exist if the system determinant is zero. This leads us to cubic algebraic equation for Ω , which is solved numerically.

ORCID

References

- A. Lasia, Electrochemical Impedance Spectroscopy and its Applications (Springer, New York) (2014).
- A. Kulikovsky, "Analytical impedance of oxygen transport in a PEM fuel cell channel." J. Electrochem. Soc., 166, F306 (2019).
- A. Kulikovsky, "Analytical impedance of oxygen transport in the channel and gas diffusion layer of a PEM fuel cell." J. Electrochem. Soc., 168, 114520 (2021).
- N. Wagner and E. Gülzow, "Change of electrochemical impedance spectra (EIS) with time during CO-poisoning of the Pt-anode in a membrane fuel cell." *J. Power Sources*, 127, 341 (2004).
- O. Antoine, Y. Bultel, and R. Durand, "Oxygen reduction reaction kinetics and mechanism on platinum nanoparticles inside Nafion." *J. Electroanal. Chem.*, 499, 85 (2001).

- R. Makharia, M. F. Mathias, and D. R. Baker, "Measurement of catalyst layer electrolyte resistance in PEFCs using electrochemical impedance spectroscopy." *J. Electrochem. Soc.*, 152, A970 (2005).
- S. K. Roy and M. E. Orazem, "Deterministic impedance models for interpretation of low frequency inductive loops in PEM fuel cells." ECS Trans., 3, 1031 (2006).
- S. K. Roy, M. E. Orazem, and B. Tribollet, "Interpretation of low-frequency inductive loops in pem fuel cells." *J. Electrochem. Soc.*, 154, B1378 (2007).
- B. P. Setzler and T. Fuller, "A physics-based impedance model of proton exchange membrane fuel cells exhibiting low-frequency inductive loops." *J. Electrochem.* Soc., 162, F519 (2015).
- C. Gerling, M. Hanauer, U. Berner, and K. A. Friedrich, "Experimental and numerical investigation of the low-frequency inductive features in differential pemfcs: Ionomer humidification and platinum oxide effects." *J. Electrochem. Soc.*, 170, 014504 (2023).
- I. A. Schneider, M. H. Bayer, A. Wokaun, and G. G. Scherer, "Impedance response of the proton exchange membrane in polymer electrolyte fuel cells." *J. Electrochem. Soc.*, 155, B783 (2008).
- K. Wiezell, P. Gode, and G. Lindbergh, "Steady-state and eis investigations of hydrogen electrodes and membranes in polymer electrolyte fuel cells: i. modeling." *J. Electrochem. Soc.*, 153, A749 (2006).
- N. Holmström, K. Wiezell, and G. Lindbergh, "Studying low-humidity effects in pefcs using eis: i. experimental." J. Electrochem. Soc., 159, F369 (2012).
- A. Kosakian, L. P. Urbina, A. Heaman, and M. Secanell, "Understanding singlephase water-management signatures in fuel-cell impedance spectra: a numerical study." *Electrochim. Acta*, 350, 136204 (2020).
- I. Pivac and F. Barbir, "Inductive phenomena at low frequencies in impedance spectra of proton exchange membrane fuel cells—A review." J. Power Sources, 326, 112 (2016).
- Q. Meyer and C. Zhao, "Air perturbation-induced low-frequency inductive electrochemical impedance arc in proton exchange membrane fuel cells." *J. Power Sources*, 488, 229245 (2021).
- A. Kulikovsky, "Effect of proton conductivity transients on PEM fuel cell impedance: Formation of a low-frequency inductive loop." *Electrochem. Comm.*, 140, 107340 (2022).
- A. Kusoglu, A. Kwong, K. T. Clark, H. P. Gunterman, and A. Z. Weber, "Water uptake of fuel-cell catalyst layers." J. Electrochem. Soc., 159, F530 (2012).
- Y. Zhang, G. Agravante, T. Kadyk, and M. H. Eikerling, "Modeling water phenomena in the cathode side of polymer electrolyte fuel cells." *Electrochimica Acta*, 452, 142228 (2023).
- W. Olbrich, T. Kadyk, U. Sauter, and M. Eikerling, "Modeling of wetting phenomena in cathode catalyst layers for pem fuel cells." *Electrochimica Acta*, 431, 140850 (2022).
- M. Eikerling, "Water management in cathode catalyst layers of pem fuel cells: a structure-based model." *J. Electrochem. Soc.*, 153, E58 (2006).
- A. Z. Weber, R. M. Darling, and J. Newman, "Modeling two-phase behavior in pefcs." J. Electrochem. Soc., 151, A1715 (2004).
- J. Zhou, A. Putz, and M. Secanell, "A mixed wettability pore size distribution based mathematical model for analyzing two-phase flow in porous electrodes." *J. Electrochem. Soc.*, 164, F530 (2017).
- A. Kosakian, F. Wei, J. Zhou, S. Jung, J. Sharman, and M. Secanell, "Impact of liquid-water accumulation and drainage cycles on fuel-cell performance and stability." *Electrochimica Acta*, 469, 143221 (2023).
- T. E. Springer, T. A. Zawodzinski, and S. Gottesfeld, "Polymer electrolyte fuel cell model." J. Electrochem. Soc., 138, 2334 (1991).
- H. Fathi, A. Raoof, S. H. Mansouri, and M. Th, "van Genuchten. Effects of porosity and water saturation on the effective diffusivity of a cathode catalyst layer." *J. Electrochem. Soc.*, 164, F298 (2017).
- I. Nazarov and K. Promislow, "Ignition waves in a stirred PEM fuel cell." Chem. Engineer. Sci., 61, 3198 (2006).
- M. Reum, S. A. Freunberger, A. Wokaun, and F. N. Büchi, "Measuring the current distribution in PEFCs with sub-millimeter resolution. ii. impact of operating parameters." *J. Electrochem. Soc.*, 156, B301 (2009).
- D. Muirhead, R. Banerjee, J. Lee, M. G. George, N. Ge, H. Liu, S. Chevalier, J. Hinebaugh, K. Han, and A. Bazylak, "Simultaneous characterization of oxygen transport resistance and spatially resolved liquid water saturation at high-current density of polymer electrolyte membrane fuel cells with varied cathode relative humidity." *Int. J. Hydrogen Energy*, 42, 29472 (2017).
- Z. Tang, Q.-A. Huang, Y.-J. Wang, F. Zhang, W. Li, A. Li, L. Zhang, and J. J. Zhang, "Recent progress in the use of electrochemical impedance spectroscopy for the measurement, monitoring, diagnosis and optimization of proton exchange membrane fuel cell performance." *J. Power Sources*, 468, 228361 (2020).